AFRL-AFOSR-VA-TR-2016-0223

High Fidelity Measurement and Modeling of Interactions between Acoustics and Heat Release in Highly-Compact, High-Pressure Flames

William. Anderson
PURDUE UNIVERSITY
401 SOUTH GRANT ST
WEST LAFAYETTE, IN 47907-2024

05/24/2016
Final Report

Air Force Research Laboratory
AF Office Of Scientific Research (AFOSR)/RTA1

Arlington, Virginia 22203
Air Force Materiel Command

REPORT DOCUMENTATION PAGE

Form Approved
OMB No. 0704-0188

Public reporting burden for this collection of information is estimated to average 1 hour per response, including the time for reviewing instructions, searching existing data sources, gathering and maintaining the data needed, and completing and reviewing this collection of information. Send comments regarding this burden estimate or any other aspect of this collection of information, including suggestions for reducing this burden to Department of Defense, Washington Headquarters Services, Directorate for Information Operations and Reports (0704-0188), 1215 Jefferson Davis Highway, Suite 1204, Arlington, VA 22202-4302. Respondents should be aware that notwithstanding any other provision of law, no person shall be subject to any penalty for failing to comply with a collection of information if it does not display a currently valid OMB control number. **PLEASE DO NOT RETURN YOUR FORM TO THE ABOVE ADDRESS.**

1. REPORT DATE *(DD-MM-YYYY)* 18-05-2016	2. REPORT TYPE Final	3. DATES COVERED *(From - To)* 12/1/13 – 2/29/16

4. TITLE AND SUBTITLE

High Fidelity Measurement and Modeling of Interactions between Acoustics and Heat Release in High-Impact, High-Pressure Flames

5a. CONTRACT NUMBER
FA9550-14-1-0020

5b. GRANT NUMBER
106862

5c. PROGRAM ELEMENT NUMBER

6. AUTHOR(S)

William E. Anderson

Stephen D. Heister

5d. PROJECT NUMBER

5e. TASK NUMBER

5f. WORK UNIT NUMBER

7. PERFORMING ORGANIZATION NAME(S) AND ADDRESS(ES)

Purdue University
401 S. Grant St.
West Lafayette, IN 47907-2024
(765) 494-1063

8. PERFORMING ORGANIZATION REPORT NUMBER

9. SPONSORING / MONITORING AGENCY NAME(S) AND ADDRESS(ES)
USAF, AFRL DUNS 143574726
AF Office of Scientific Research
875 N. Randolph St. Room 3112
Arlington, VA 22203

10. SPONSOR/MONITOR'S ACRONYM(S)
AFOSR

11. SPONSOR/MONITOR'S REPORT NUMBER(S)

12. DISTRIBUTION / AVAILABILITY STATEMENT
Unclassified/Unlimited distribution

13. SUPPLEMENTARY NOTES

14. ABSTRACT

The defining characteristics of advanced chemical propulsion systems include very high rates of volumetric energy deposition, and very small combustor sizes. These characteristics give rise to extremely compact interactions in space and time between the chamber acoustic modes and unsteady heat release modes that may result in combustion instability. This project seeks to better understand the coupling mechanisms between heat release, hydrodynamics, and acoustics, and to develop tools to study the problem. High-fidelity simulations using large eddy simulations and reduced reaction kinetics are providing insight into unsteady reacting flows at an unprecedented level, providing some hope that *a priori* predictions will be possible in the next decade. Important questions include the accuracy of prediction that is required, and the level of modeling that is required for that prediction. The simulations must also be validated with experimental data. However, the time and length scales, and energy deposition rates in the canonical laboratory flames that have been studied over the past two decades are orders of magnitude different than the environments encountered in practical rocket combustors. The main objective of this study is to obtain high-fidelity experimental data critically needed to validate research codes at relevant conditions, and to develop systematic and rigorous means for comparison.

15. SUBJECT TERMS
combustion stability, validation, rocket engine

16. SECURITY CLASSIFICATION OF:			17. LIMITATION OF ABSTRACT	18. NUMBER OF PAGES	19a. NAME OF RESPONSIBLE PERSON William Anderson
a. REPORT	b. ABSTRACT	c. THIS PAGE	UU		19b. TELEPHONE NUMBER *(include area code)* 765-496-2658

Standard Form 298 (Rev. 8-98)
Prescribed by ANSI Std. Z39.18

High Fidelity Measurement and Modeling of Interactions
between Acoustics and Heat Release in Highly-Compact,
High-Pressure Flames W.E. Anderson, Purdue University

The defining characteristics of advanced chemical propulsion systems include very high rates of volumetric energy deposition, and very small combustor sizes. These characteristics give rise to extremely compact interactions in space and time between the chamber acoustic modes and unsteady heat release modes. The very tight coupling combines with high energy release rates to make the study and mitigation of combustion dynamics in rocket engine combustors a very challenging problem. Research is needed to better understand these tightly-coupled interactions, and to develop tools to study the problem.

High-fidelity simulations are providing insight into unsteady reacting flows at an unprecedented level, providing some hope that *a priori* predictions will be possible in the next decade. The present state-of-the-art in research computations use large eddy simulations combined with reduced reaction kinetics and models for turbulent combustion. Important questions include the accuracy of prediction that is required, and the level of modeling that is required for that prediction. The simulations must also be validated with experimental data. However, the time and length scales, and energy deposition rates in the canonical laboratory flames that have been studied over the past two decades are orders of magnitude different than the environments encountered in practical rocket combustors. The main objective of this study is to obtain high-fidelity experimental data critically needed to validate research codes at relevant conditions, and to develop systematic and rigorous means for comparison.

Introduction

The issue of combustion instability is a common recurring problem for bi-propellant rocket engines. Decades of successful operation of rocket combustors has failed to yield a complete understanding of combustion instability. [53,46] Instabilities arise due to coupling between the natural acoustic modes of a combustor and the unsteady processes of combustion. High-frequency combustion instabilities in excess of 1000 Hz are detrimental to combustor performance and lead to catastrophic failures in engines due to over-pressure and overheating. Engine geometry is strongly correlated with the formation of instabilities, and, as a result, a complete characterization of this complex process may only be obtained during full scale testing to completely represent the engine's acoustic properties. If the stability characteristics of the engine can be adequately modeled, large savings can be made in the cost of engine development.

Currently available modeling techniques and technologies do not allow for complete simulation of a full scale engine. Recently, however, high-fidelity CFD models have shown some ability of being able to match stability behavior in subscale experimental combustors. [42] By developing techniques to accurately model subscale experiments, those techniques could then be applied to full scale engines to allow prediction of combustion stability at an early phase in engine design. Modeling and experimentation aims to generate lower order combustion characterization functions from high fidelity, experimentally validated CFD models. These functions could then be applied to engine designs early in the design process to predict and mitigate potentially catastrophic combustion instability effects. This coalescence of experimentation and model validation should produce a complete and powerful model of combustion instability for rocket and other propulsion systems.

High fidelity CFD models required for unstable combustion require huge amounts of computational power. Modeling flow physics alone on length and time scales small enough to resolve critical flow mechanisms limits the capabilities of recent models. As a result, simplified chemical kinetics models are used to represent very complex combustion chemistry. It has been suggested that a detailed chemistry model is required to accurately capture the heat release process that is so critical to the development of an unstable combustion environment.

Testing of CFD models by experiment is an integral step in developing tools to predict and mitigate combustion instability in engine design. The transfer of energy from the combustion of propellants to the acoustic energy field is the primary mechanism that creates acoustically coupled combustion instability. Chamber acoustics as predicted by high fidelity models show excellent agreement to experimental data, but direct comparison of the combustion energy release is more challenging. A direct measurement of heat release in a practical combustor is not feasible and measurement techniques that do not interfere with the flame itself are limited. Collection of light emitted from chemiluminescent species in the flame is commonly employed to estimate locations of high heat release. This

technique relies on several fundamental assumptions, such as the spatio-temporal coincidence of light emission and heat release, optical depth of the flame, and three-dimensional effects, all of which were addressed in this study.

The focus of this study is the stability behavior of a sub-scale rocket combustor with a single shear coaxial injector element. A brief history of previous research on the flame under investigation and a survey of investigations on chemiluminescence as a heat release indicator are presented. Building on experiments involving an optically accessible combustion chamber, the recent study focuses on improving the quantitative nature of optical measurements and gaining insight on the use of combustion light emission as an indicator of heat release. The report describes the experimental and modeling approach used to investigate the heat release and chemiluminescent species distributions in a highly unstable flame. Results of spectroscopic imaging of the combustion light emission are compared to results from a detailed chemical kinetics model of the unstable flame. Finally, conclusions on the suitability of this approach for model validation for the subject flame are presented.

Approach

Experiment

As described previously, the CVRC test article has been used extensively to produce data sets for comparison to high fidelity CFD models. [54,38,6,17] The CVRC was designed to investigate the stability characteristics of an oxidizer centered shear-coaxial type injector element, common to oxidizer rich staged combustion engines, in a self-excited unstable combustion environment. The oxidizer post length can be varied continuously during a test by changing the axial position of an orifice plate within the post. It has been shown that the oxidizer post length plays a critical role in the stability of the injector element. In model validation experiments, the combustor burns decomposed 90% concentrated hydrogen peroxide and gaseous methane at a total equivalence ratio of 0.8, total mass flow rate of 0.345 kg/s, and average chamber pressure of 1.4 MPa. Although CFD modeling of the CVRC is performed using an oxidizer post length of 14 cm, in experimentation the oxidizer post length can be varied from 19 cm to 8.9 cm or fixed at any length in between. For translating oxidizer post tests, the post length is assumed to be quasi-static for small time intervals for comparison to computational models in which the geometry is fixed. In all cases in this discussion the oxidizer post length is 14 cm, a length associated with high amplitude instability. Figure 1 shows the combustor configuration. Head end chamber sections are interchanged dependent upon the type of measurements being performed.
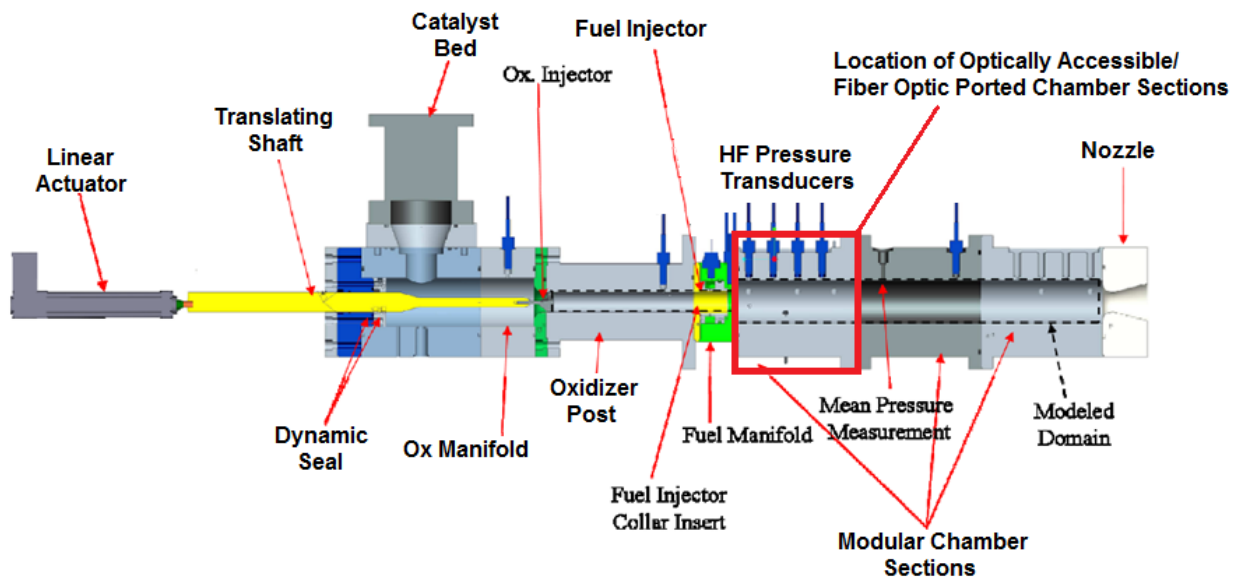

Figure 1: Cross-section view of the CVRC test article. The focus of optical measurements is the combustor head end highlighted in red.

Previous investigations of chemiluminescence in the CVRC combustor involved line of sight imaging of the combustor head end at 10 kHz frame rates through a fused quartz combustion chamber segment and filters designed to optically band pass filter emitted light around wavelengths associated with OH* and CH* chemiluminescent emissions near 309 nm and 431 nm respectively. The results offered 2-D line-of-sight integrated spatial and temporal trends in relatively large wavelength bands of emitted light. The images suffered relatively low spatial resolution due to obscuration by the quartz glass combustor wall, and distortion from intensified imaging equipment required to collect emission signals in the UV-Visible spectrum.

For improved spatial resolution of optical measurements and to increase the quantitative nature of the results, broadband spectral imaging of the CVRC combustion emission was performed using a fiber optic-coupled imaging spectrometer. The head end chamber section was replaced with one allowing integration of a 400 micron diameter fused silica fiber optic probe allowing collection of UV-Vis light emission. Several ports in the chamber allowed for line-of-sight light collection through the center-line of the combustion zone at various axial locations. As installed, the field of view of the fiber probe has an included angle of approximately 6.75 degrees extending 45 mm across the chamber diameter resulting in a probe volume of 717.2 mm^3. The probe coupled light into a Horiba Scientific iHR550 imaging spectrometer with entrance slit width of 0.2 mm. The spectrometer was configured with a 150 g/mm diffraction grating resulting a spectral range of 265-470 nm for the detector used, capturing both OH* and CH* emission bands. Spectra were imaged at 10,000 samples/sec using a high speed UV intensifier and CMOS detector. The configuration of the spectroscopic imaging equipment is shown in Figure 2: Configuration of spectroscopic imaging equipment. The chamber segment used for fiber optic sensing also allowed for installation of high frequency pressure transducers at axial locations coincident to fiber probe locations enabling direct observation of the phase difference between pressure oscillations and light emission.
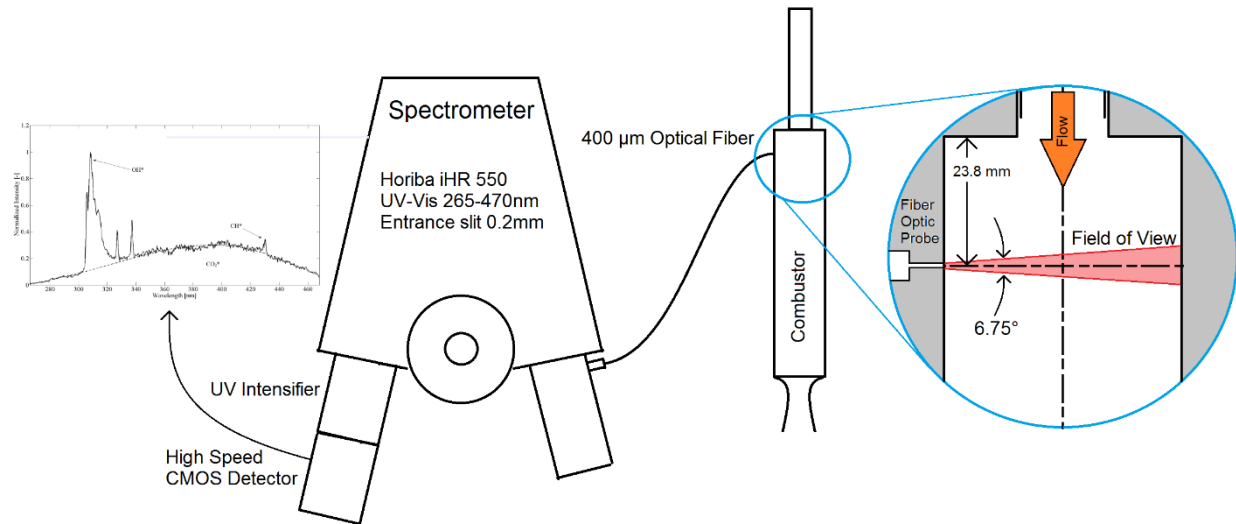

Figure 2: Configuration of spectroscopic imaging equipment.

The fiber probe chamber section with an overlay representing the average heat release as predicted by hybrid RANS-LES modeling by Harvazinski [17] is shown in Figure 3. In this study, spectra and pressure data were collected from optic port 3 located 23.8 mm downstream of the injector dump plane for direct comparison to computational model data. Optical and pressure data were also collected at the port 5 location 31.6 mm downstream of the injector dump plane to allow for investigation of spatial differences from the port 3 location.
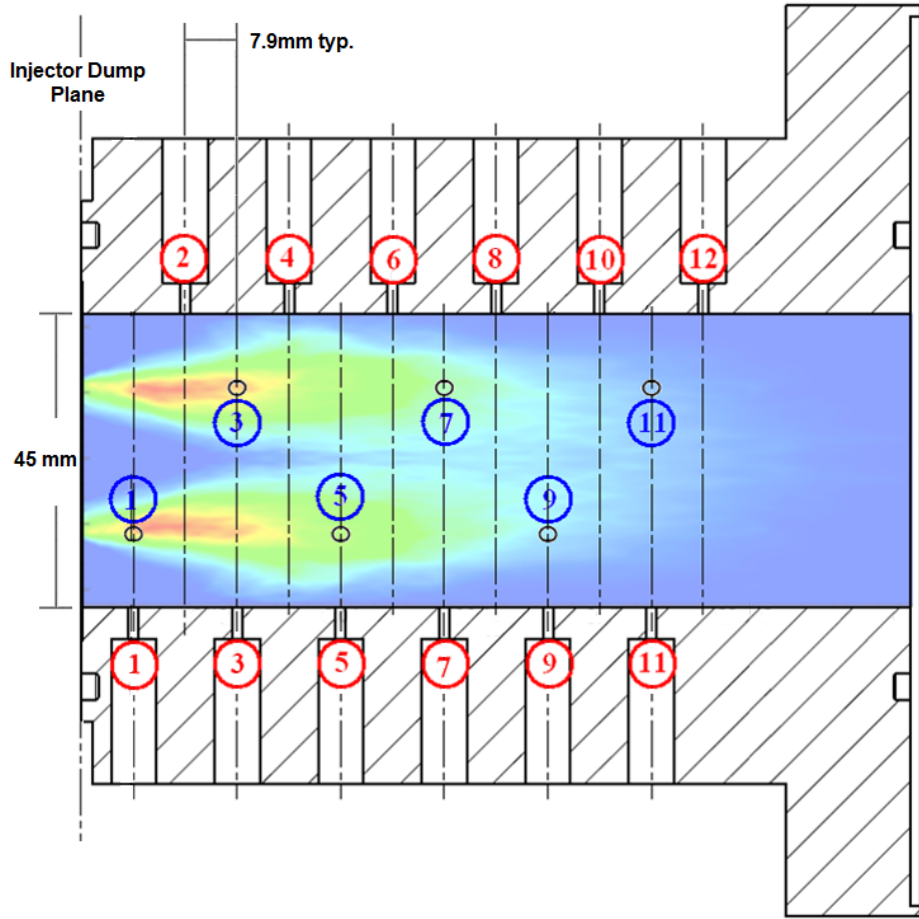
Figure 3: Head end chamber section with optical ports labeled in red and high frequency pressure measurement ports labeled in blue. Primary data collection for comparison to computations was from optical port 3 while a secondary dataset was acquired from port 5 for relative spatial comparisons. The contour plot represents time averaged heat release based on a 3-D hybrid RANS-LES model using a global chemical kinetics model.

Results

Experiment

A typical test of the CVRC begins with a period of oxidizer only flow to allow the hydrogen peroxide catalyst bed to reach operating temperature. Fuel flow is initiated and ignition is achieved by injection of a 12 mL JP-8 slug at 10 seconds. Translation of the oxidizer post choke plate begins at 11 seconds, reducing the oxidizer post length from 19 cm to 8.9 cm over 2 seconds during bipropellant operation prior to shut down. Pressure data recorded from the combustor head end are shown in Figure 4. The transition to unstable operation occurs at 12 seconds when the oxidizer post length is approximately 14.5 cm. The spectrogram of head end pressure in Figure 4 shows the transition to unstable operation and the corresponding oxidizer post length. The pressure oscillation amplitude is approximately 1 MPa with a fundamental frequency of 1312 Hz. The pressure oscillation is characterized by a steep-fronted pressure rise followed by a more gradual expansion as shown in Figure 5 with several smaller peaks caused by reflected waves and higher modal frequencies. Pressure measurements at several axial locations in the combustor and oxidizer post indicate traveling pressure waves, rather than standing waves, are present in the combustor at high oscillation amplitudes. This behavior is also observed in computational models [44,17].
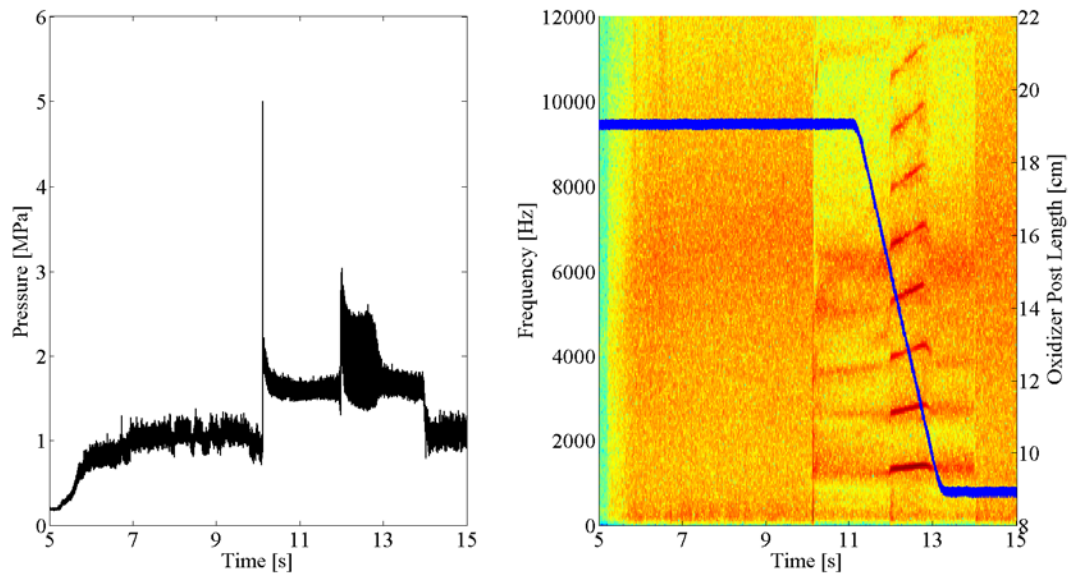
Figure 4: Typical chamber pressure trace for CVRC test (left) and spectrogram showing frequency content in the chamber pressure signal over the course of the test. The blue line overlaid on the spectrogram represents the length of the oxidizer post as it is translated from the 19cm configuration to the 8.9cm configuration.
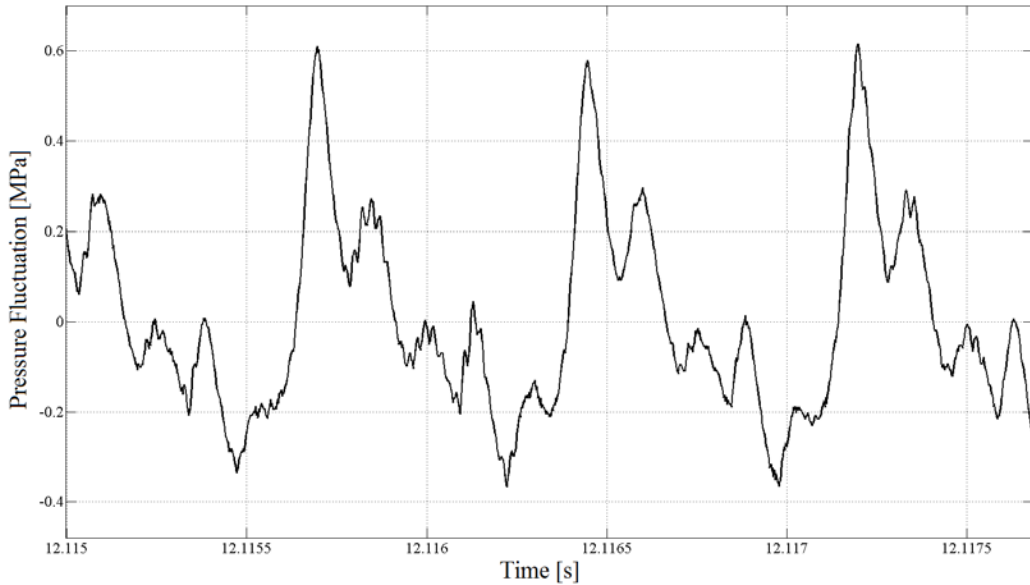

Figure 5: Typical pressure fluctuation trace [MPa] near the injector dump plane of the CVRC combustor during limit cycle operation.
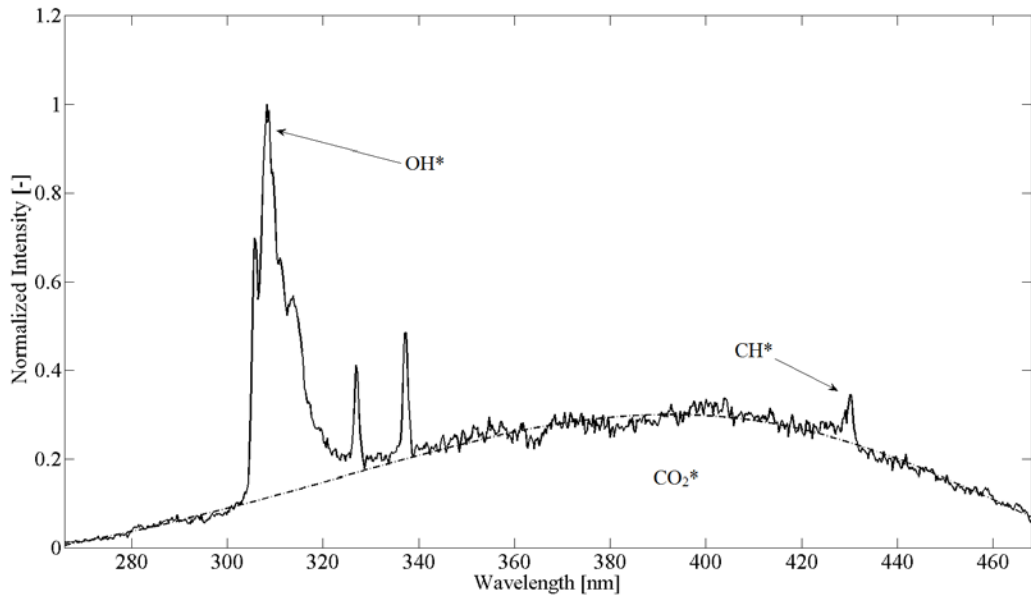
Figure 6: Average emission spectrum captured from the optic port 3 location. The most intense emissions are from OH* and CH* emissions near 309nm and 431nm respectively. A broadband emission from CO₂* is observed for the full spectral width of the measurement. Two intense lines appear near 328nm and 338nm due to emission from atomic silver entrained in the oxidizer flow from the hydrogen peroxide catalyst bed.

The average emission spectrum collected by the fiber optic probe during unstable operation of the CVRC is shown in Figure 6. The average spectrum indicates a strong emission from the $A^2\Sigma^+ \to X^2\Pi$ transition of OH* near 309 nm. Emission from the $A^2\Delta \to X^2\Pi$ transition of CH* near 431 nm is significantly lower in average intensity, and light emission in this wavelength range is dominated by broadband CO₂* emission as expected from a high pressure lean flame. Two strong peaks at 328 nm and 338 nm are emission from atomic silver [49] that is eroded from the hydrogen peroxide catalyst bed. The spectrum is corrected for variation in the quantum efficiency of the imaging hardware over the wavelength range of interest.

To relate the unsteady heat release field to the strongly resonant flow, it is most useful to consider pressure phase locked average signals of light emission, thus averaging cycle-to-cycle variability caused by random turbulence in the flame. Phase averaging was performed over 25 pressure oscillation periods at the first longitudinal acoustic mode frequency of 1312 Hz. A cubic spline interpolation was performed to generate 50 data points per oscillation period and averaging was performed at each of these points. Although continuously translating, the average oxidizer post length during this interval is 14 cm, a thoroughly studied unstable configuration for the CVRC [54,38,6,17]. Phase averaged emission spectra and pressure signals from chamber port location 3 are shown in Figure 7.
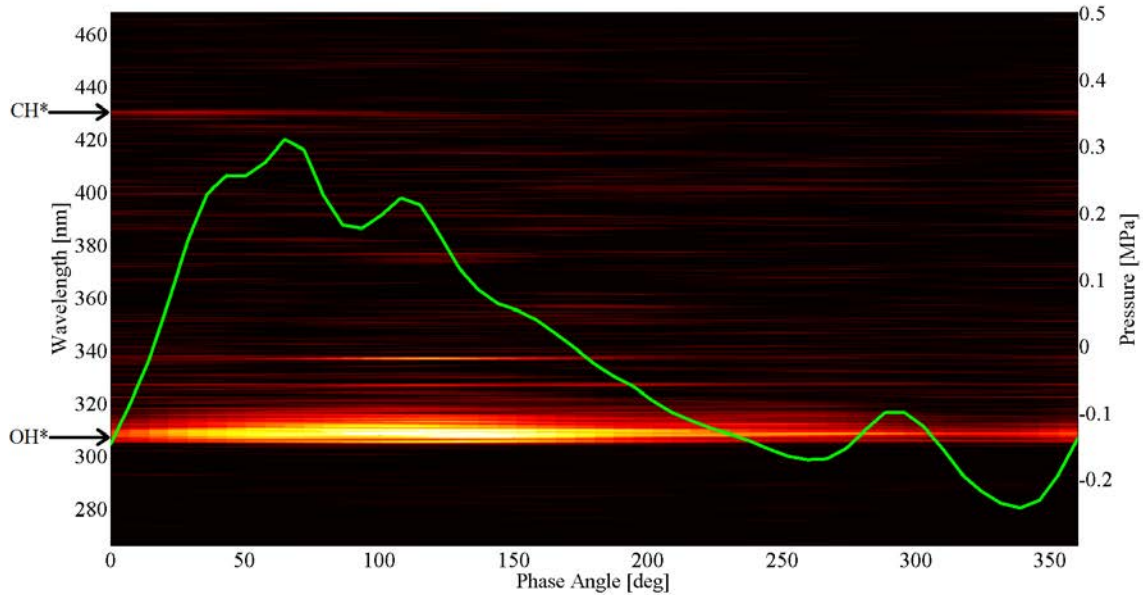
Figure 7: Phase averaged pressure fluctuation (green) and spectral emission signals (background) from the CVRC optical port 3 location. Emission from CO_2 has been subtracted to highlight locations of OH* and CH* emissions.*

To compare the relative intensities of the OH* and CH* emission signals, the CO_2* background emission was assumed to be self-similar and was approximated by a fifth order polynomial as shown by Lauer [27] and subtracted from the spectra. It is evident in these spectra that the CH* emission signal is only slightly more intense than the noise level, but is still detectable despite the high pressure conditions of the flame. The phase averaged OH* and CH* emission signals are plotted against the phase averaged pressure signal at port location 3 in Figure 8. Comparison of the light emission and pressure signal shows that the peak OH* emission lags the peak pressure by about 40° while the peak CH* emission leads the peak pressure by about 50° on average. Thus, the total phase difference between peak OH* and CH* chemiluminescence is about 90°. Figure 8 also shows the phase averaged pressure and OH* and CH* emission signals from the port 5 location (15.8 mm downstream from port 3). Note that the general trend between the two locations is consistent. The CH* emission reaches a maximum just ahead of the passage of the pressure peak, while the peak OH* emission lags behind the pressure maximum.
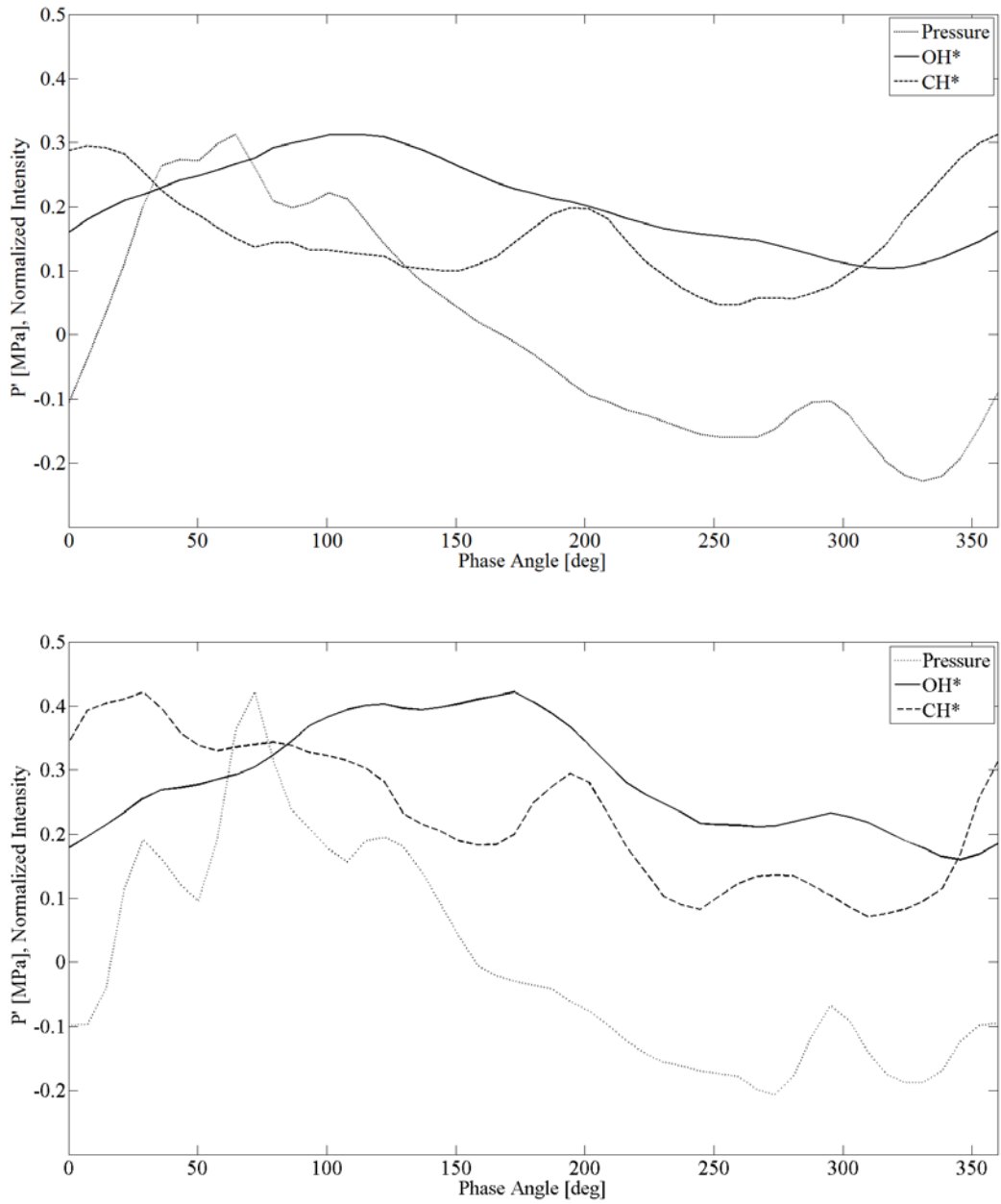
Figure 8: Phase averaged pressure and OH* and CH* emission as measured from the port 3 location (top) and the port 5 location (bottom)

Simulations

Background

The gaseous fuels, choked boundary conditions, and wide range of instability amplitudes make the CVRC experiment amenable to modeling. Significant modeling work has been done by a variety of groups using hybrid RANS/LES models [44,18,19] and large eddy simulations [11,45]. All prior simulations have used global or 2-step

reduced mechanisms. In general two-dimensional simulations were unable to replicate the instability amplitudes seen in the experiment while three-dimensional simulations produced excellent agreement with the experiments for the unstable operating conditions. The stable and marginally stable operating conditions have been more difficult to match. Prior work by Harvazinski et al. has suggested that the instability is caused by the timing of the reflected pressure wave in the oxidizer post and its interaction with a cyclic fuel supply cut off event [19].

It is widely known that global and highly reduced chemical kinetics introduce large approximations to the actual combustion processes. Global mechanisms are typically tuned to match specific parameters, like ignition delay or laminar flame speed. Because only a few tunable parameters exist in the model it is not possible to match all relevant parameters over a wide range of operating conditions. Combustion in the CVRC is highly complex, regions of premixed, non-premixed, and partially premixed combustion exist at different times and locations of the combustor. Local extinctions and re-ignitions are also present and are key to the instability mechanism. The timing of all of these events is either closely coupled with the chamber acoustics in the unstable case or not coupled in the stable case. These observations suggest that it is necessary to evaluate the effects of including detailed chemical kinetics mechanisms on the prediction of combustion instabilities. This is the objective of the present work. Specifically, we compare the simulations with detailed kinetics with those done with simplified global kinetics to ascertain the differences in the physics of coupling between the combustion and acoustic cycle. All three oxidizer post-length cases are studied and attention is paid to discerning the specific modes of coupling that lead to the incidence of combustion instability. The mechanisms used for methane oxidation are the GRI 1.2 set that comprises of 32 chemical species and 177 reactions. All the computations performed here use an axisymmetry assumption in order to accommodate the detailed chemical mechanisms efficiently. The computations utilize detached eddy simulations to capture the turbulence in the flame region with laminar combustion closure, consistent with our previous studies using global chemical kinetics.

Gas Phase Reaction Kinetics

Modeling of the CVRC experiment using CFD has been previously attempted by several researchers [43,18,11,45]. All of these simulations are similar in that they used simplified reaction mechanisms. Before proceeding with the simulations, detailed analysis of four methane combustion mechanisms is presented. The simplest mechanism is a single global reaction where the fuel and oxidizer react to form water and carbon dioxide. The production of carbon monoxide is a known intermediate step in hydrocarbon oxidation and is included in the two-step reduced mechanism. In both the mechanisms, the rate expressions were calibrated to measured laminar flame speeds [51]. GRI-1.2 is a more complete set of hydrocarbon reactions consisting of 177 reactions involving 32 species and was optimized for natural gas combustion at the Gas Research Institute (GRI) [9]. A further refinement of the GRI-1.2 mechanism resulted in GRI-3.0, which includes nitrogen chemistry and greater number of species and reactions. In the CVRC experiment, decomposed hydrogen peroxide is the oxidizer and no nitrogen is present so GRI-3.0 is included for comparison only. All the models discussed here are readily available in literature. The models are summarized in Table 1.

Table 1. Details of the chemical kinetics mechanisms

Mechanisms→	Global-1	Global-2	GRI-1.2	GRI-3.0
Species	CH4, O2, CO2 and H2O	Global-1 species + CO	33	53
Reactions	1	2	177	325

In the CVRC, fuel at room temperature is injected upstream of the back step, along the periphery of the hot oxidizer flow as shown in Figure 9. Mixing in this region has been identified as a crucial step of the cyclic heat release process. Furthermore, hot products of combustion, trapped in the recirculation near the back step interact with the cold shear layer as shown in the schematic Figure 9. The state of the mixture therefore varies significantly and the ensuing heat release varies accordingly. To assess the chemical kinetics mechanism three parameters which correspond to the above behavior are investigated. The parameters are the ignition delay, heat release rate, and maximum temperature.
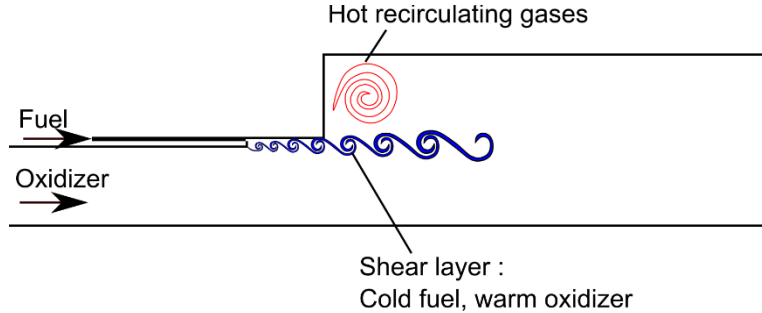
Figure 9: Schematic of flow dynamics in the CVRC Experiment. Fuel-oxidizer mixing in the region shown affects the heat release.

Ignition Delay

Figure 10 shows the ignition delay predictions of the four mechanisms considered as a function of the initial temperature of the mixture and the composition, at a constant pressure of 1.4 MPa. The temperature range applicable to the CVRC is between 1000 K and 1400 K. The lower limit represents 7% by mass of the fuel mixed with the oxidizer. The upper limit is 30% by mass of the combustion gases at 2400 K mixed with the oxidizer and fuel mixture. This range of initial temperatures shows that the ignition delay values predicted by both the global mechanisms are an order of magnitude lower in the range of interest. A similar observation has been reported in the literature [21] for a different oxidizer and operating conditions. The global two step mechanism also shows unrealistic ignition delay trend for the rich mixture. Both the detailed mechanisms show ignition delay values of the same order and are closer for near stoichiometric mixtures and at high temperatures.
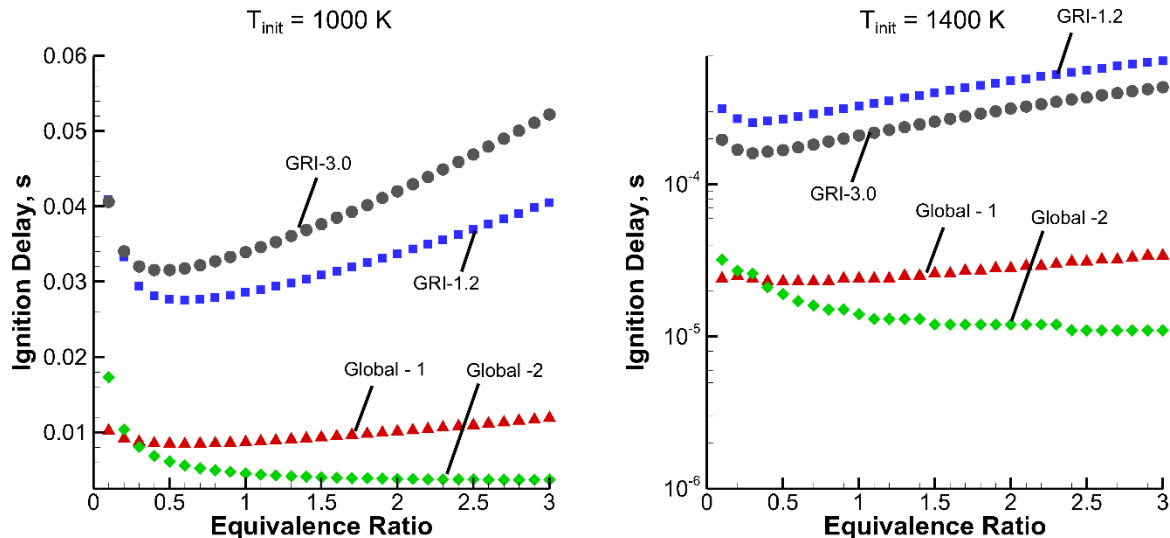

Figure 10: Variation of ignition delay predictions by the four chemical kinetics mechanisms.

Temperature

The global mechanisms predict a higher temperature rises from combustion because many intermediate and trace species are neglected. Figure 11 shows the variation in the maximum temperature prediction by the four mechanisms. In the plots the maximum temperature is normalized by the initial temperature. It is clear that the peak temperatures predicted by the global mechanisms exceed those of the detailed kinetics by a factor of 1.3 to 1.5. This affects not only the speed of sound in the mixture but also the interaction between the burnt and unburnt mixtures. The combination of the shorter ignition delay and higher post-flame temperature can initiate combustion earlier in the mixing region which will delay the further mixing of fuel and oxidizer. In two-dimensional simulations the effect would be magnified because of the axisymmetry assumption and may entirely prevent the further mixing of fuel and oxidizer. As a result, this would lead to a stretched heat release zone.
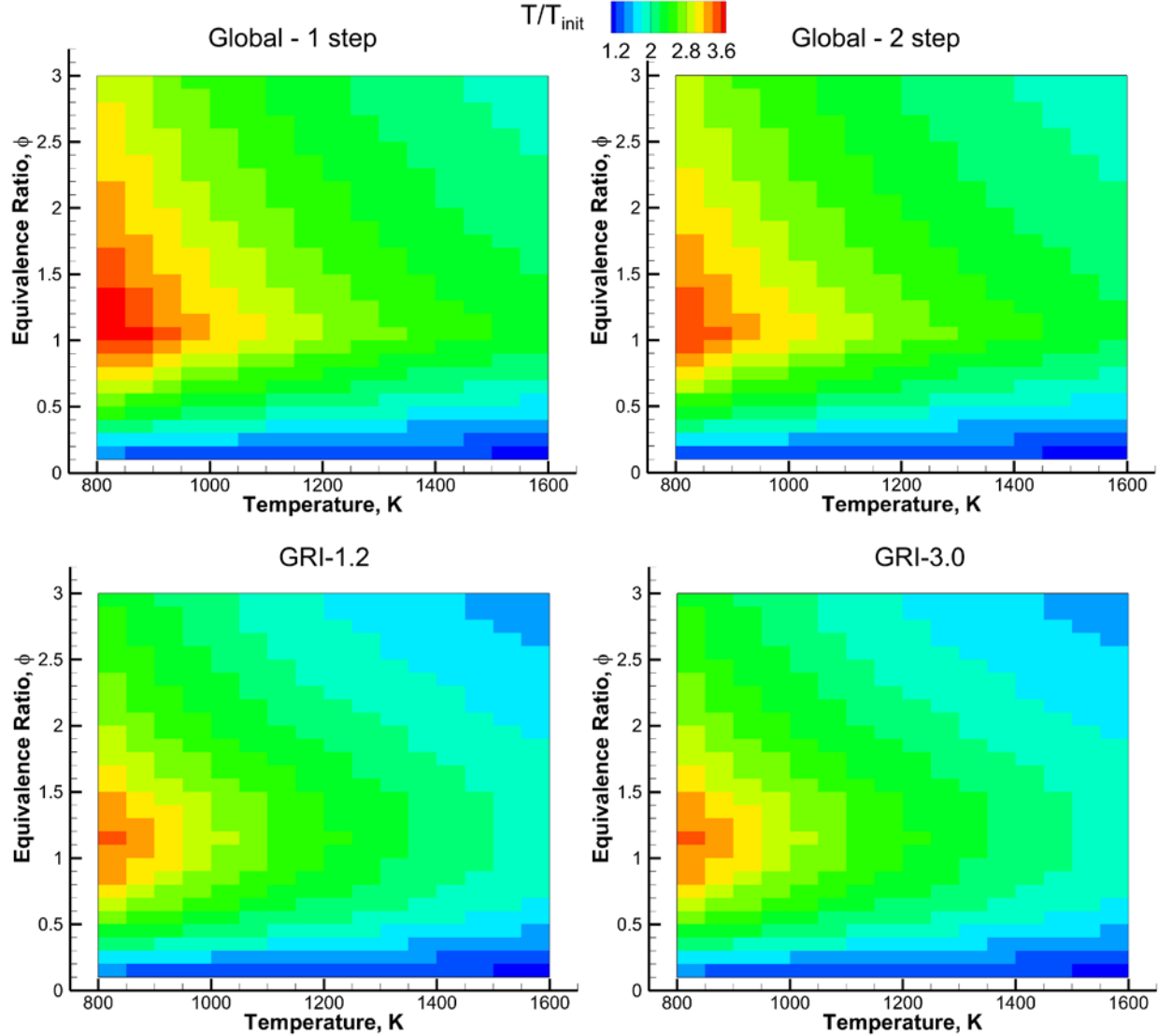
Figure 11: Variation of normalized maximum temperature predictions by the four chemical kinetics mechanisms.

Heat Release Rate

Combustion instability prediction is closely related to the heat release rate prediction and its coupling with the acoustic modes. Figure 12 shows the comparison of the maximum heat release rates for the global-1 and GRI-1.2 mechanisms under consideration. Predictions of the GRI-3.0 and global-2 are close to those shown for GRI-1.2 and global-1 mechanisms respectively. The heat release rate predictions of the global mechanisms exceed those of the detailed kinetics by an order of magnitude and can significantly over predict the heat release rate, which influences acoustic fluctuations. It is likely that these differences along with those mentioned earlier can materially affect the nature of the combustion stability mechanisms.

Amongst the above results, it is notable that the temperature prediction of the detailed mechanisms is nearly identical. The ignition delay predictions of the two detailed mechanisms are close and the heat release of the GRI-3.0 mechanism, although not shown, resembles the predictions of the GRI-1.2 mechanism. These similarities can be attributed to the fact that the GRI-3.0 mechanism has evolved from the GRI-1.2 mechanism. The GRI-1.2 mechanism is therefore expected to give similar results as the GRI-3.0 mechanism. The remaining results in the report therefore consider only the GRI 1.2 mechanism and make comparisons with the global-1 mechanism that was used in previous studies.
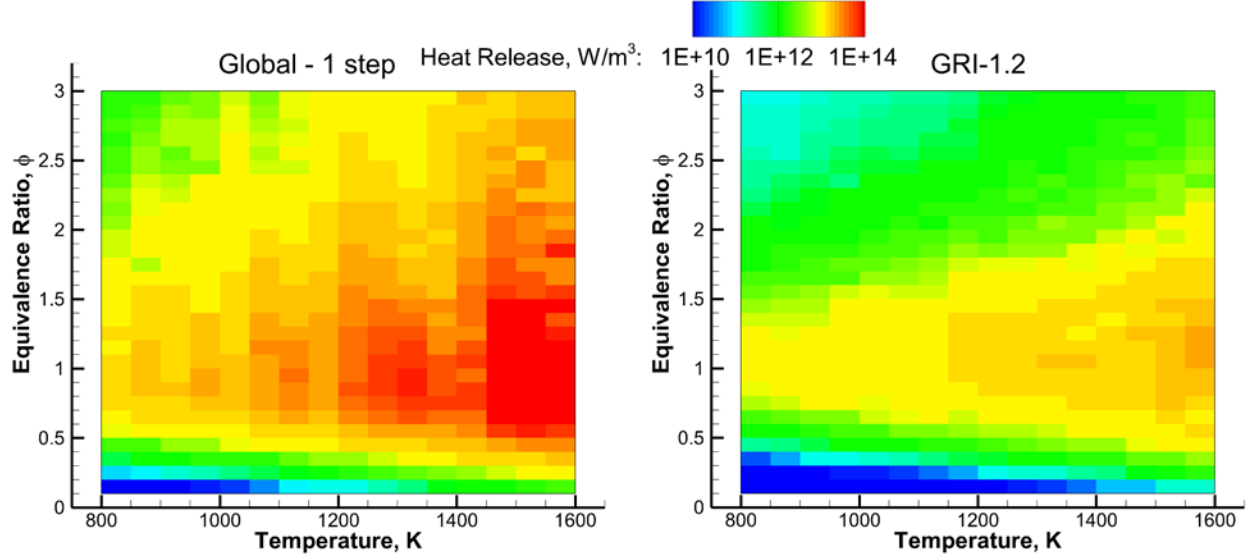
Figure 12: Variation of maximum heat release rate predictions by the two chemical kinetics mechanisms.

Consistent with the previous work, the CFD code GEMS (General Equation and Mesh Solver) is employed in the present work for the computational investigation. GEMS solves the implicitly discretized fully-coupled conservation equations. Dual time stepping is used to eliminate approximate factorization errors. The algorithm is second order accurate in both space and time. Large scale turbulent motions are captured in GEMS with LES (Large Eddy Simulation) while the small scales are modeled using Wilcox's k-omega model [52], which becomes dominant in the near wall region. Additional details of the code and capabilities can be found in [17,3,47,28,29].

Simulation Results and Discussion

Three cases encompassing the variations of the oxidizer post length are chosen for the study. The three oxidizer post lengths are 8.89 cm, 13.97 cm and 19.05 cm, which correspond to the marginally stable, unstable and stable operating conditions. The overall operating condition is fuel lean, with fuel to oxidizer ratio by mass of 0.85 or equivalence ratio of 0.72. A choked nozzle at the downstream boundary of the combustor creates a pressure anti-node. Likewise, the inlet oxidizer flow is choked through a series of slots, which are approximated by a constant mass flux computation in the present calculations. Adiabatic, non-slip walls are assumed for the fuel and oxidizer post as well as for the chamber walls.

 The experimental measurements include pressure probes located along the length of the combustion chamber. For comparison with the computations, the pressure probe located at the anti-node near the downstream end of the combustor is chosen for its reduced susceptibility to local variations and ability to capture limit cycle behavior. An overall comparison of experimental and computed pressure trace for the three oxidizer post lengths is shown in Figure 13, Figure 14 and Figure 15. Both the global reaction and the detailed chemical kinetics show limit cycle behavior in all the cases shown. The pressure signals from the global-1 simulations show more noise compared to the GRI-1.2 simulations. Importantly, in the case of the two shorter oxidizer post lengths, the signal correspondence between experiment and simulations is improved along with the peak-to-peak amplitude of the pressure. Particularly, for the highest amplitude instability case at a length of 13.97 cm, the detailed kinetics result agrees remarkably well with the experimental peak-to-peak magnitude, while the global-1 result appears to under-predict this by more than 50%. Predictions for the longest oxidizer post length exceed the observed magnitude of the instability. It should however be recognized that there is some modulation in the experimental pressure. The peak-to-peak pressure variation shows a maximum difference of 200 kPa, which is comparable to the global kinetics predictions.
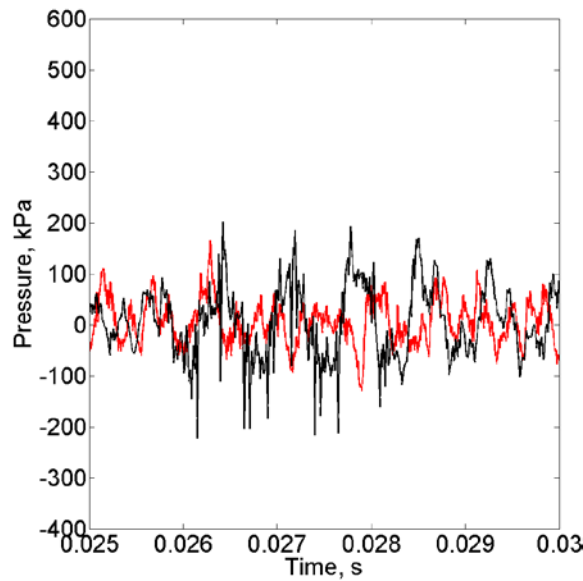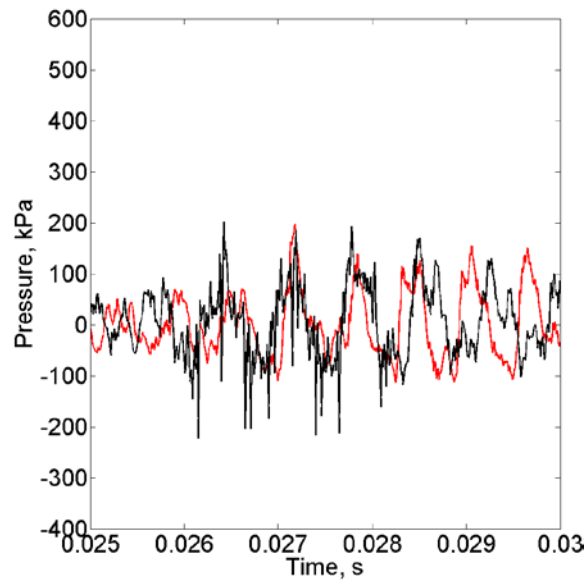
Figure 13: Pressure trace comparison with experiment. Pressure measured at the combustor wall, 36.83 cm from the combustor back step, oxidizer post length = 8.89 cm. Black: experiment, red: simulation.
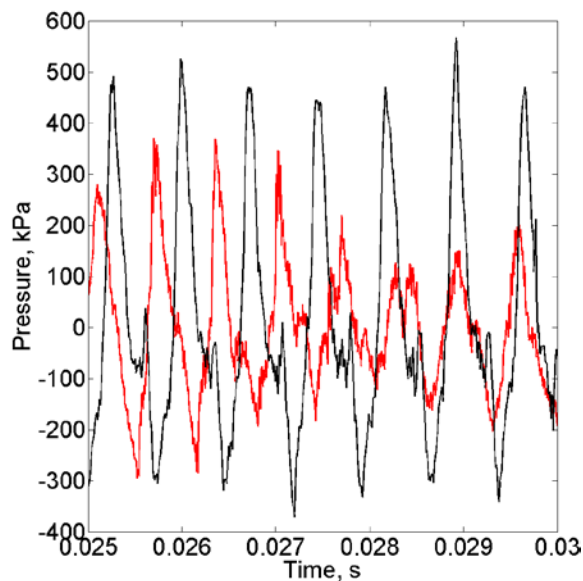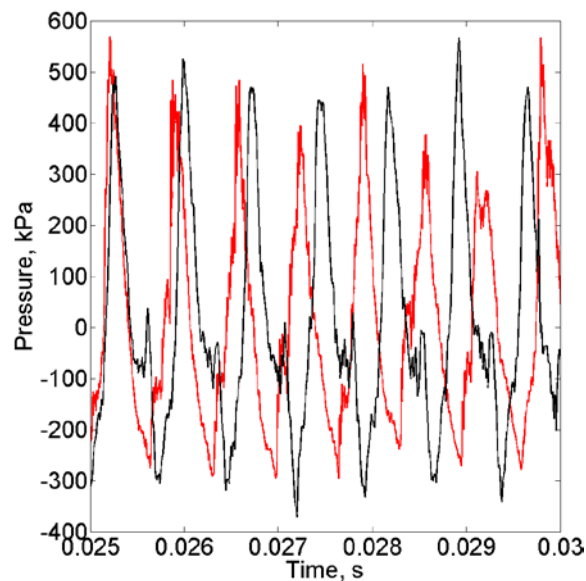
Figure 14: Pressure trace comparison for the two reaction mechanisms, oxidizer post length of 13.97 cm. Black: experiment, red: simulation.

(a) Global-1   (b) GRI-3.0
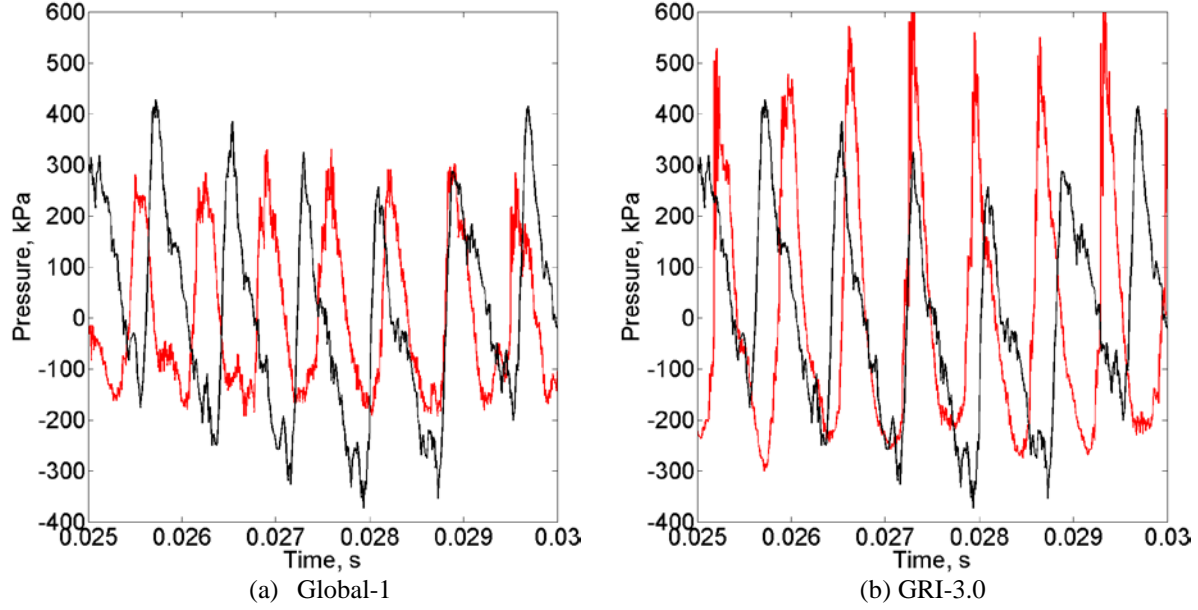
Figure 15: Pressure trace comparison for the two reaction mechanisms, oxidizer post length of 19.05 cm. Black: experiment, red: simulation.

Frequency content and the power corresponding to the dominant pressure modes is considered next and is shown in Figure 16, Figure 17, and Figure 18 for the three oxidizer post lengths. In all three cases, the global kinetics result shows that the frequency of the first acoustic mode is over-predicted by about 15-20%. In contrast, the detailed kinetics results appear to be improved with the frequency predictions now being about 10% higher than the experiments. This improvement is due to the reduction in equilibrium temperature of the flame (and reduction in the sound speed) on account of the intermediate, high heat-of-formation chemical species included in the detailed kinetics. The remaining frequency discrepancy is probably due to the use of an adiabatic wall boundary; the inclusion of the wall heat flux would likely further reduce the temperature and the sound speed and, consequently, the acoustic frequency. It is also evident that the amplitude of the modes are also improved by the inclusion of detailed kinetics, especially in the case of the two unstable lengths - i.e., post-lengths of 13.97 cm and 19.05 cm. An exception to this is the second mode of the 13.97 cm, which is predicted to be about the same for both the global and detailed kinetics cases. Still, one might note that the general trend is that the detailed kinetics predictions show sharper resolution of the higher harmonics, even if the amplitudes continue to be somewhat under-predicted.


(a) Global-1   (b) GRI-3.0
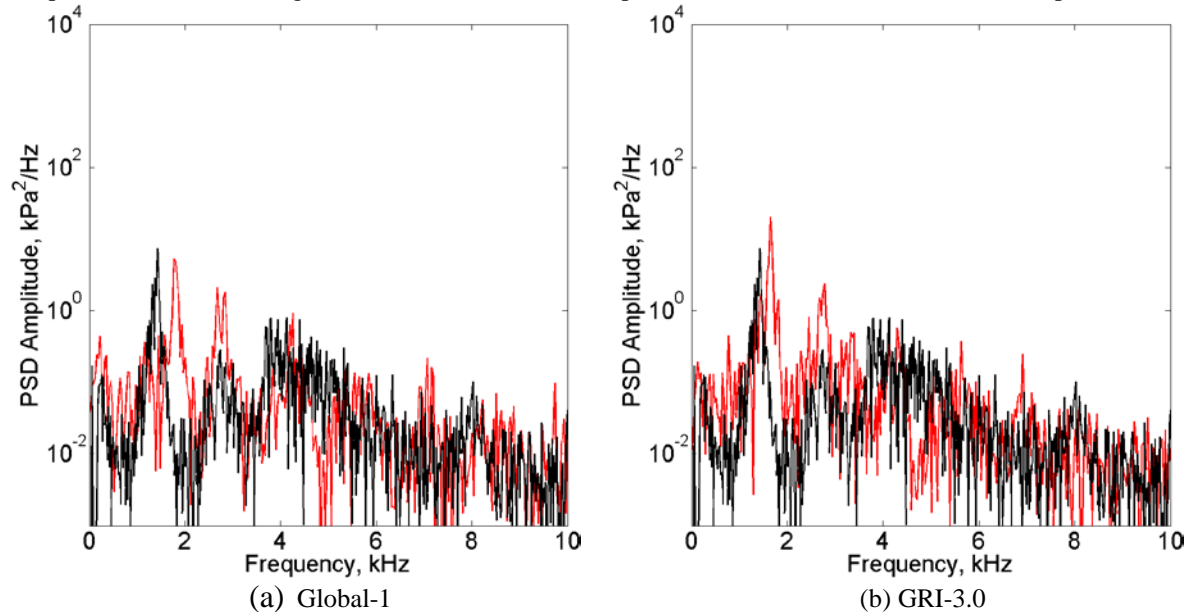
Figure 16: Power spectral density comparison for the two reaction mechanisms, oxidizer post length of 8.89 cm. Black: experiment, red: simulation.


(a) Global-1   (b) GRI-3.0
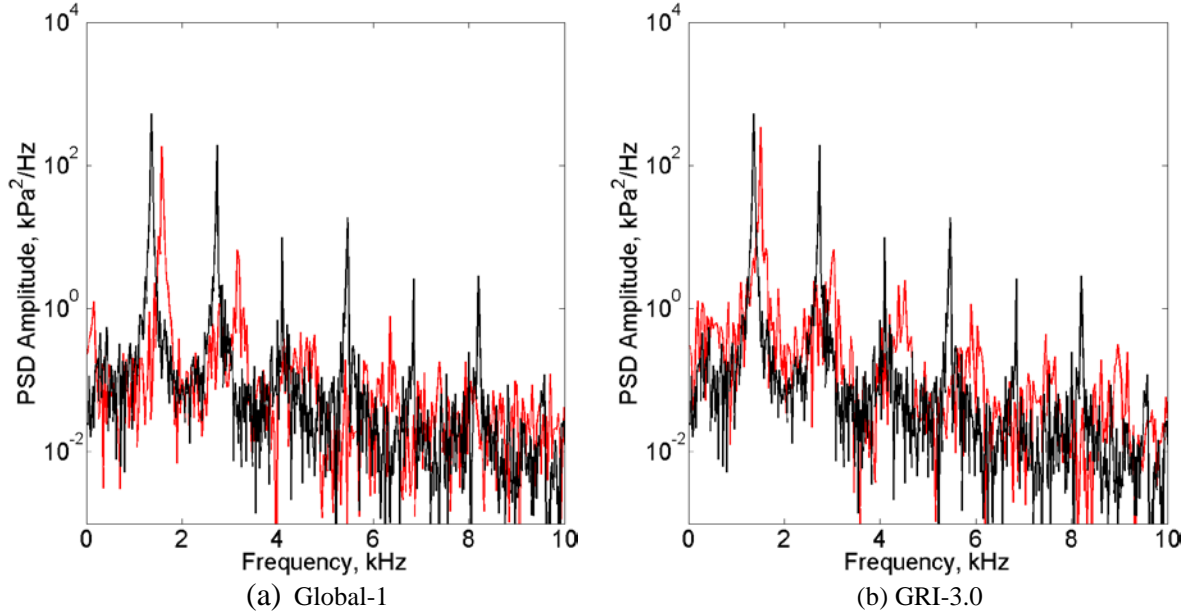
Figure 17: Power spectral density comparison for the two reaction mechanisms, oxidizer post length of 13.97 cm. Black: experiment, red: simulation.


(a) Global-1   (b) GRI-3.0
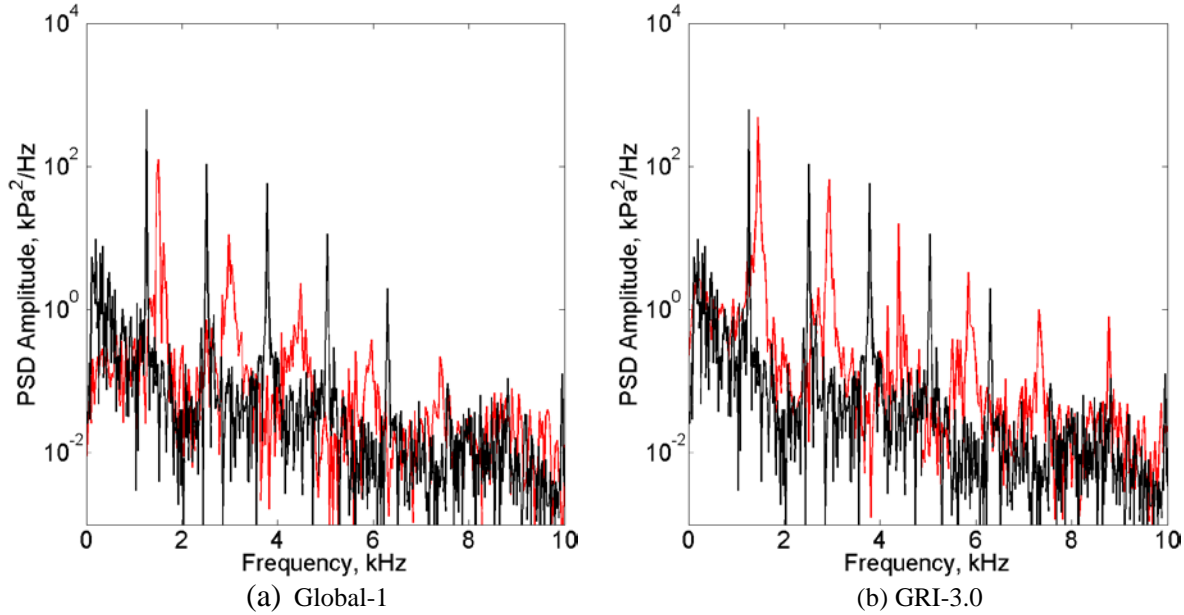
Figure 18: Power spectral density comparison for the two reaction mechanisms, oxidizer post length of 19.05 cm. Black: experiment, red: simulation.

In addition to these comparisons, the simulations can also aid in developing the understanding of the physics involved in the unstable combustion with the two longer oxidizer post lengths and clarify possible differences in the case of marginally stable shorter oxidizer post length. The following subsections present detailed results from each of the oxidizer post lengths, the unstable operating condition is considered first.

Unstable Operating Condition

Experimental chemiluminescence images of the near back step combustion behavior through two radical species CH* and OH* have been obtained for all three oxidizer post-lengths. Both of the species have been used as markers of heat release in various experiments [34,20], but modeling of these radicals has been limited to relatively simple flames [36] and rare in multi-dimensional simulations [48]. A major difficulty in their inclusion as a computed species lies in the absence of their source species in the kinetics mechanisms that are typically used for the simulations. With the detailed kinetics like the GRI-1.2, this no longer is the case and both CH* and OH* can be computed as quasi-steady species in a post-processing step with minimal computational cost. The assumption of quasi-steadiness can be expected to be better held for the CH* than OH* because of its lower concentrations [34].

Phase averaged pressure cycle at the head end of the combustor is shown in Figure 19. Corresponding visual comparison is shown in Figure 20. The experimental images are CH* radicals. The images are inverse Abel transformed to account for line of sight measurements and phase averaged to diminish cycle to cycle variations. Simulation images are from axisymmetric computations and are similarly phase averaged. At the start of the cycle, during pressure rise, high intensity emission is seen near the wall of the combustor. At or near the peak pressure (cycle point 3), the high intensity region displays a shift away from the wall. Pressure in the head end decreases from cycle points 7 to 15, while the luminosity of the CH* radicals indicates reduced number density. Towards the end of the cycle, points 18 to 20 show increasing intensity, marking the beginning of the next cycle. The same structural sequence can be seen in the computed CH* radical. The results suggest that the sequence of events starts with a partially mixed fuel-oxidizer jet hitting the combustor wall and rolling up to form two vortices. The upstream vortex interacts with the corner recirculation zone near the back step of the combustor. The hotter corner recirculation zone being on the periphery of the fuel-oxidizer mixture in the shear layer, forms a high concentration CH* region. A more detailed cycle analysis with the help of computational results of the global-1 and GRI-1.2 mechanisms is presented next to illustrate the differences.
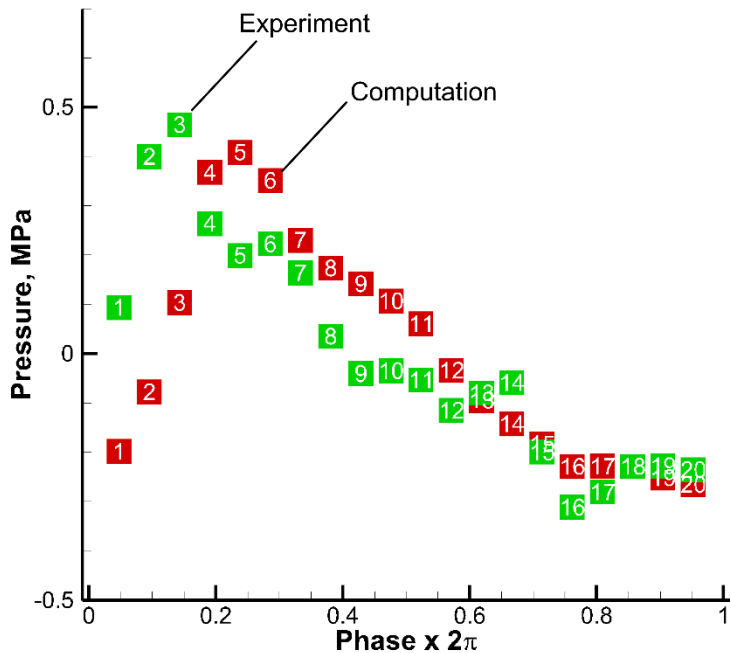

*Figure 19: Comparison of phase averaged pressure cycle at the head end.*
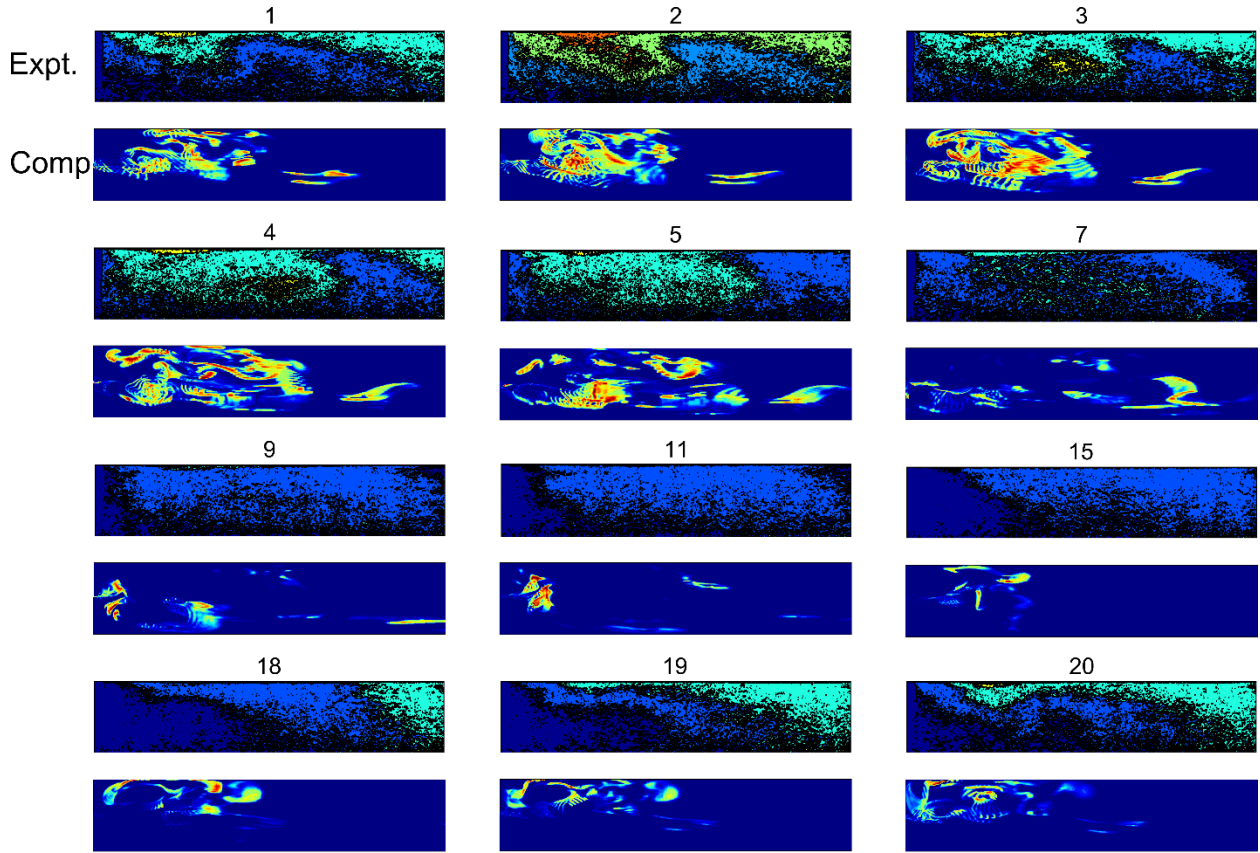
Figure 20: Comparison of selected inverse Abel transformed CH* radical images from the experiments and the computations

To understand the coupling between the unsteady heat release and the acoustics of the combustor, captured by GRI-1.2 mechanism, a representative cycle is selected for analysis. The pressure at the head end for the cycle is shown in Figure 21. Five points are marked on the cycle for both the global-1 and GRI-1.2 mechanism. Corresponding detailed contour plots showing the pressure, heat release, fuel mass fraction and axial velocity are included sequentially, beginning with Figure 22.

High pressure at the start of the cycle is generated near the back step of the combustor due to intense heat release near the head end of the combustor. Corresponding decrease in the accumulated fuel can be seen for the GRI-1.2 result. A similar effect is absent in the global-1 simulation. This difference can be attributed to diminished mixing, which occurs due to direct conversion of fuel to the final combustion. In the downstream section of the combustor, the hot combustion products drive the axial velocity, leading to enhanced mixing. High temperature in this region accelerates the consumption of the residual fuel. The pressure wave generated travels upstream in the oxidizer post, reducing the velocity and fuel-oxidizer mixing near the lip of the co-axial injector.
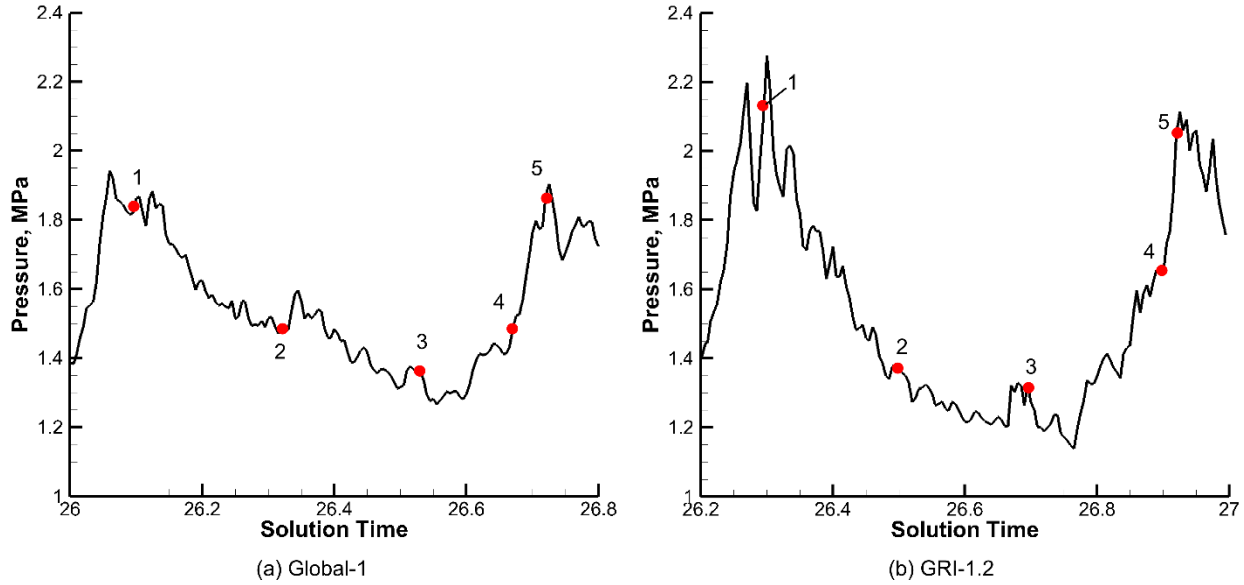
Figure 21: Pressure cycle chosen for detailed analysis of the oxidizer post length 13.97 cm
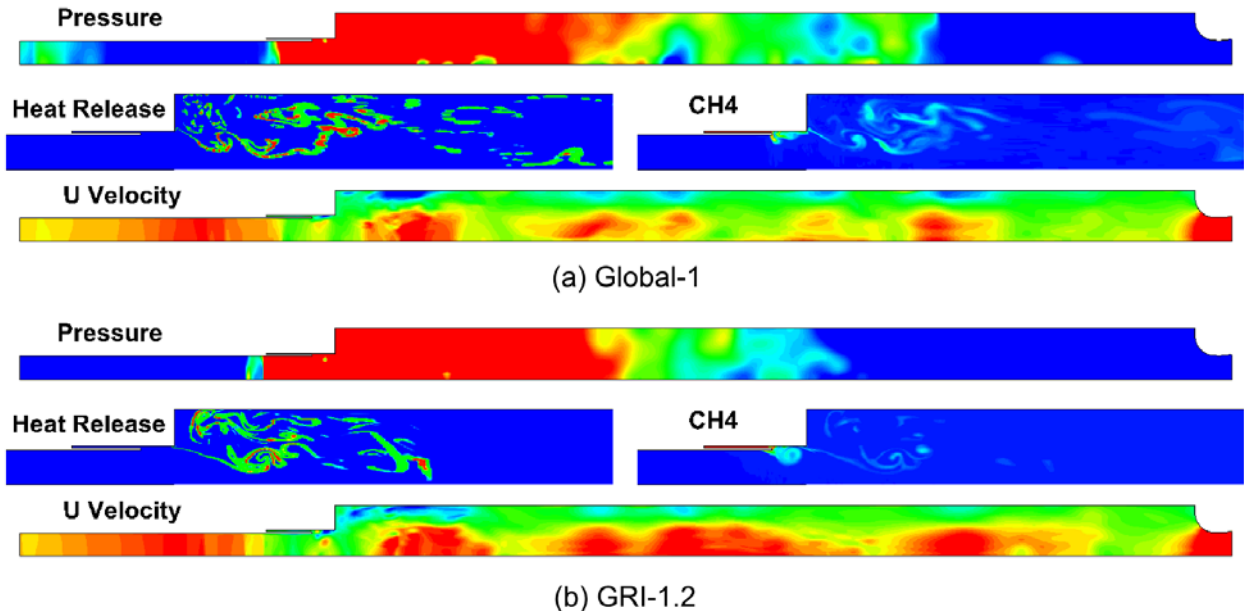

Figure 22: Limit cycle analysis: time-1 for oxidizer post length of 13.97 cm. The scales are - pressure: 1.4 to 1.6 MPa; heat release: 0.01TW/m3 to 1TW/m³; fuel mass fraction: 0 to 1 and velocity: -200 to 400 m/s.

Contour plots corresponding to the second point of the cycle are shown in Figure 23. Following the previous point in the cycle, the high pressure at the head end decreases. The rapid fuel consumption in the downstream section of the combustor, along with reduced mixing in the oxidizer post cuts off the fuel supply to the reaction zone. In this respect, a clear distinction between the predictions of the global-1 mechanism and the GRI-1.2 mechanism can be seen. Whereas the global-1 mechanism, owing to unreacted fuel and oxidizer, shows continued heat release; the GRI-1.2 mechanism shows reduced heat release, marking the fuel cut-off. As a result, drop in the head end pressure in the case of GRI-1.2 predictions is greater than the global-1 predictions.
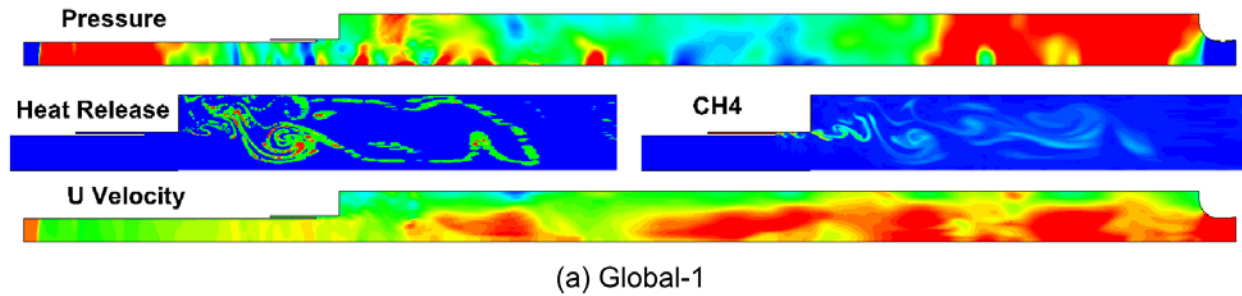
(a) Global-1
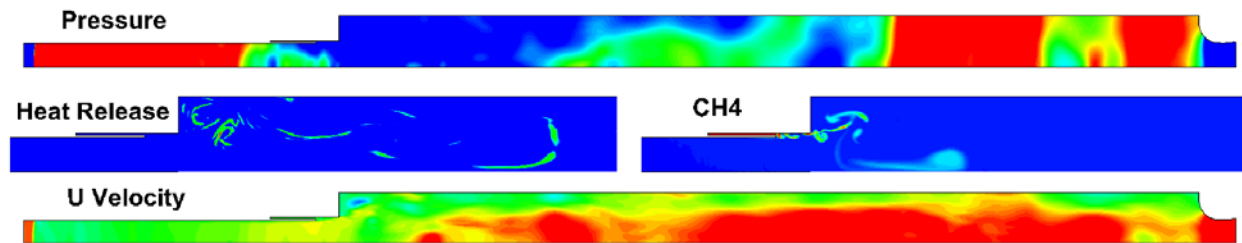
(b) GRI-1.2

Figure 23: Cycle point – 2, oxidizer post length of 13.97 cm.

Additionally, the results with GRI-1.2 mechanism show that the high velocity products move downstream, reducing shear near the back step. This allows incoming fuel and oxidizer to continue with limited entrainment of the hot products from corner recirculation zone. The relatively colder fuel stream forms an outward curving jet. In contrast, presence of heat release in the case of global-1 mechanism implies hot gas ingestion in the shear layer near the back step. A shorter ignition delay in case of the global-1 is therefore exacerbated.
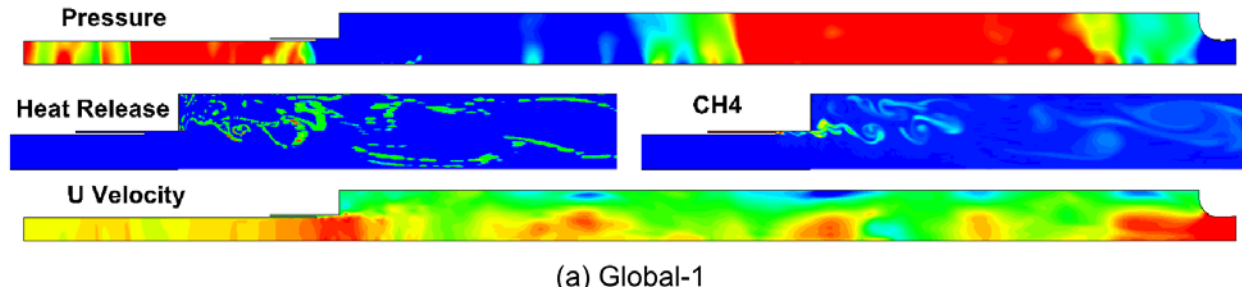

(a) Global-1
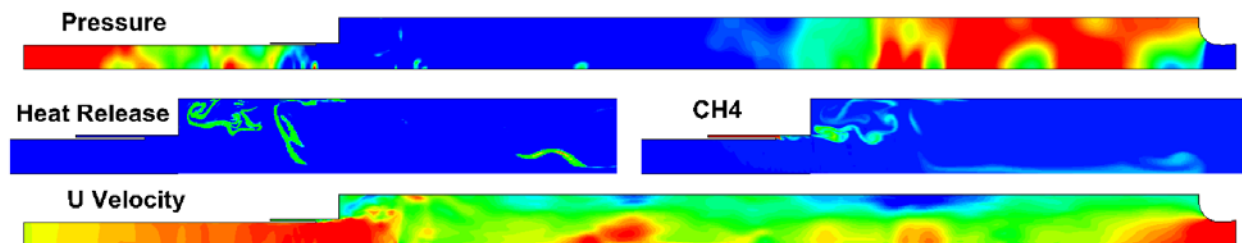
(b) GRI-1.2

Figure 24: Cycle point – 3, oxidizer post length of 13.97 cm.

Figure 24 shows the next point in the cycle. The combination of reduced mixing and fuel cut-off from the reaction zone allows the fuel in the combustor to remain unreacted. Arrival of the reflected pressure wave from the oxidizer post near the lip of the fuel sleeve causes greater shear and enhances mixing. At the back step, fuel roll up is enhanced due to higher shear induced by increased velocity. At this time, the fuel jet shown in the previous instance is broken to form two vortices; upstream and downstream of the break-up location. This is easily perceived from the GRI-1.2 results. The upstream vortex squeezes the shear layer near back step to further enhance the hot gas

ingestion. Notably, the formation of this vortex and its interaction with the shear layer is better visualized in the GRI-1.2 results. Since the incipient fluid dynamics is largely influenced by heat release rate and location, the global-1 predictions lack in this case.

The next point in the cycle is shown in *Figure 25*. There are significant differences at this point between the predictions of global-1 mechanism and GRI-1.2. The most easily seen is the location and structure of the heat release. Global-1 mechanism predicts smaller, less contiguous heat release zones compared to the GRI-1.2, which shows a large coherent structure nearer the back step of the combustor. Formation of this structure is a result of the backward movement of the roll-up vortex generated during the previous instance due to arrival of the reflected pressure in the combustor. Higher fuel consumption in the case of GRI-1.2 is another point of difference that remains throughout the cycle. More subtle difference is the higher pressure upstream in the oxidizer post as well as downstream in the combustor. The heat release during the cycle is responsible for generating pressure waves and continued heat release with global-1 mechanism is likely the reason for the observed difference in the pressure at the extremities.
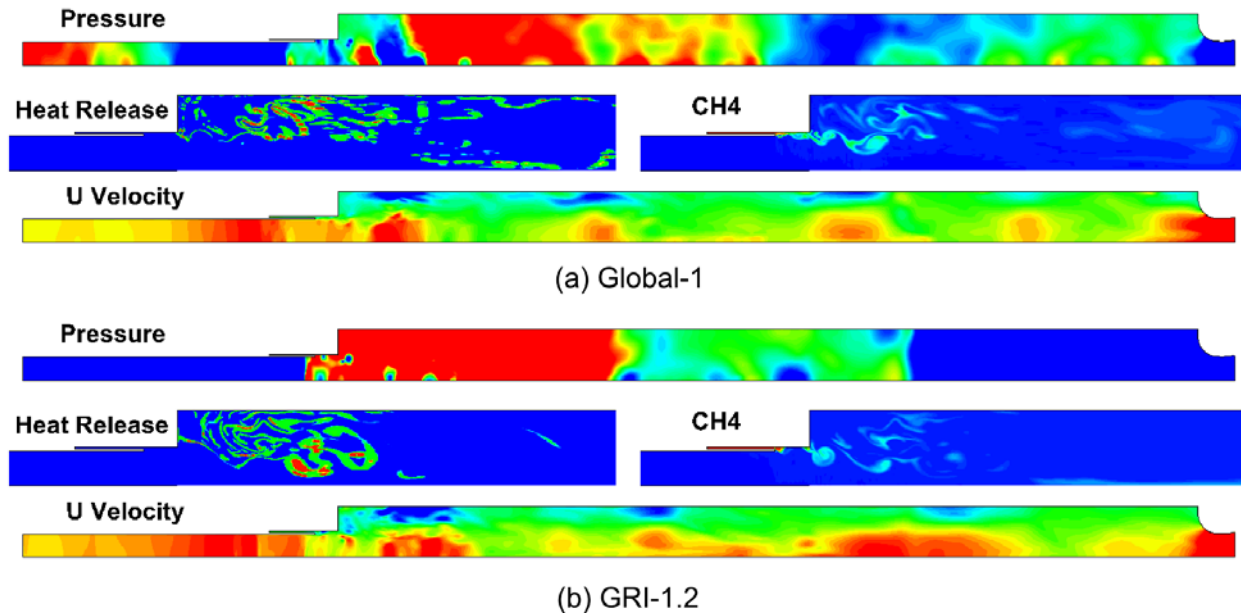

Figure 25: Cycle point – 4, oxidizer post length of 13.97 cm.

(a) Global-1

(b) GRI-1.2
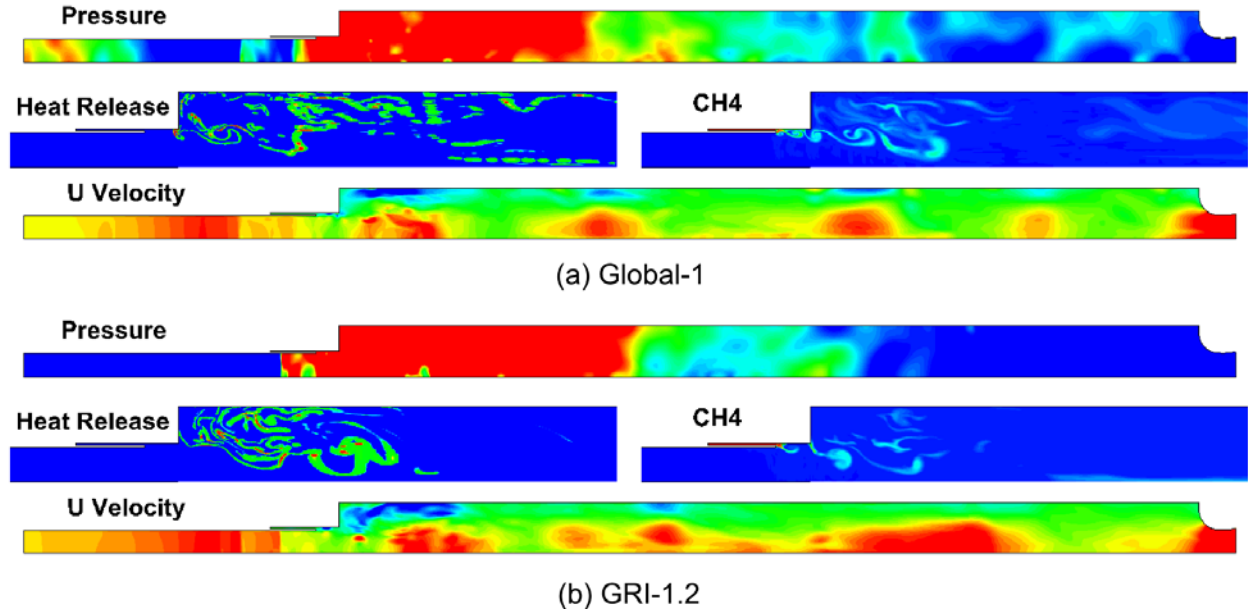
Figure 26: Cycle point – 5, oxidizer post length of 13.97 cm.

The last point in the cycle analysis is depicted in Figure 26. A major difference between the heat release and fuel consumption can be observed at this point. The fuel consumption and heat release near the head end section of the combustor in the case of GRI-1.2 mechanism is higher than that predicted by the global-1 mechanism. Consequently, the predicted pressure rise in that section is also higher and hence the incoming fuel forms a vortex moving towards the axis of the combustor. This radially inward movement of the fuel allows for better mixing with the oncoming oxidizer. This mixture burns partially due to higher residence time in this section. The products formed accelerate the flow both axially and radially, preventing the upstream fuel from feeding the reaction zone, effecting a cut-off as described in the analysis of the first cycle point.

Figure 27 shows variation in local equivalence ratio (Φ) between the limits of $\Phi = 0.35$ and $\Phi = 3.5$ at this instance. The shear layer is clearly seen from the scatter-plot, wherein the data points are sized with local equivalence ratio and colored by temperature of the mixture. Top edge of the shear layer displays high temperatures on account of its interaction with the recirculating hot products. The ignition delay in this region therefore is expected to be orders of magnitude smaller in comparison to the bottom edge of the shear layer. The unreacted fuel from the bottom edge of the shear layer, with temperature close to that of the oxidizer, follows the formation of the upstream vortex along its periphery. Recalling the variation of the ignition delay in the rich branch of the mixture and with temperature (Figure 10), burning in the shear layer and the upstream vortex will largely be controlled by mixing.

As a qualitative measure of unmixedness in this region, the standard deviation of the equivalence ratio is shown in Figure 28 as a time series along with the pressure. A clear trend is visible, a drop in the standard deviation or increased uniformity of the mixture leads to a rapid pressure rise. Accumulation of the fuel can also be deduced from this plot. Increasing unmixedness at a given temperature implies greater overall ignition delay. Increased induction period permits better mixing and partial conversion of the fuel. It must be kept in mind that the significant difference between global kinetics and detailed kinetics is the partial conversion, which can allow coherent heat release from mixtures at different states.
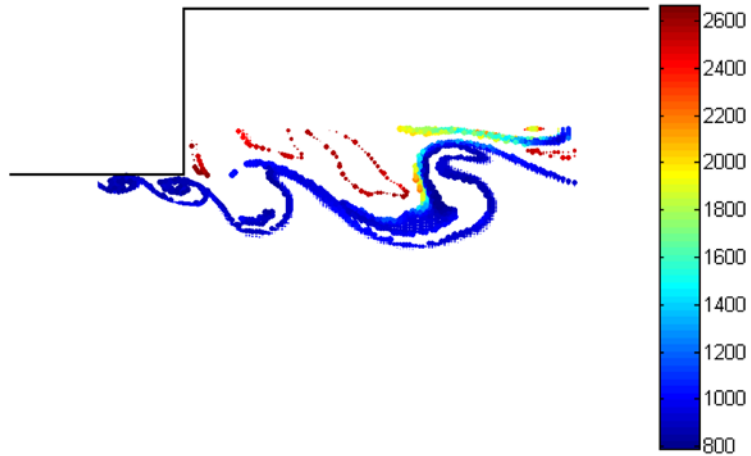
Figure 27: Shear layer, sized by local equivalence ratio and colored by temperature of the mixture. Predictions with GRI-1.2 kinetics.
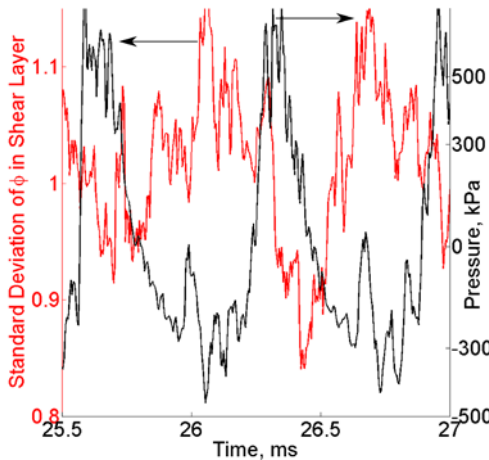

Figure 28: Unmixedness in the shear layer captured by standard deviation of the equivalence ratio.

Marginally Stable Operating Condition

The shorter oxidizer post length (8.89 cm) is a marginally stable operating point for the CVRC experiment. It is therefore of interest to contrast the findings of the unstable and marginally stable simulations with the GRI-1.2 kinetics. Comparisons of phase-averaged pressure is shown in Figure 29. The phase-averaged pressure cycle shows that the fluctuation amplitude is 20% of the unstable case. Experimental pressure indicates a similar trend as the unstable case marked by sharp pressure rise at the beginning of the cycle and a smaller increase near the bottom point of the cycle. Computations show an amplitude of pressure fluctuations lower than the experiments by factor of 2. Qualitatively the computations capture a similar effect. Especially the later part of the cycle shows smaller pressure rise at the bottom point of the cycle. Initial pressure rise shows a delay in comparison to the experiments, in addition to smaller peak value. There is also an intermediate pressure rise captured in the simulations, which is not apparent in the corresponding data. A possible reason for this discrepancy could be the axisymmetry assumption, which precludes movement in the azimuthal direction.

Figure 30 compares the experimental chemiluminescence with computed CH* species. The obvious difference between the unstable case (oxidizer post length of 13.97 cm) and the marginally stable case is the presence of chemiluminescent species throughout the cycle. Although the computations show greater variation during the cycle, it is significantly lower in comparison to the unstable case. Both the computations and experiments in the marginally stable case thus indicate sustained heat release during the cycle. Furthermore, the highest heat release during the computational pressure cycle occurs at the second pressure peak. This behavior can be further clarified from the cycle analysis below.
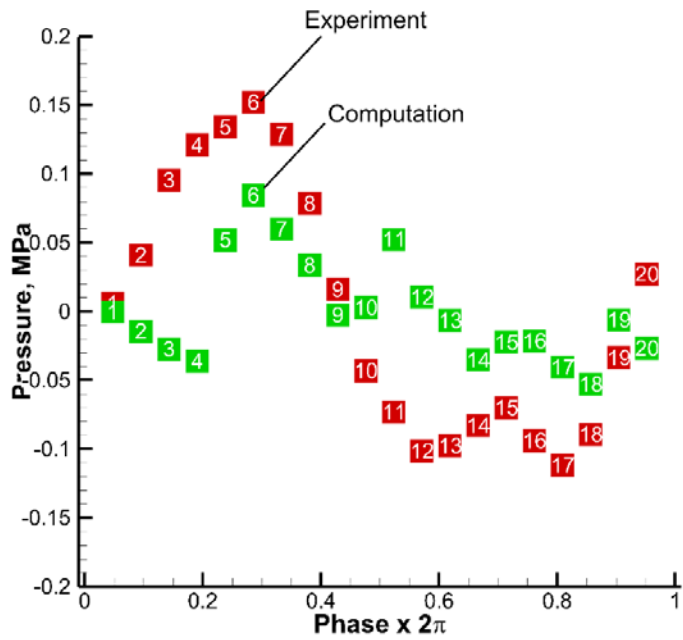
*Figure 29: Phase averaged pressure cycle for marginally stable oxidizer post length of 8.89 cm.*
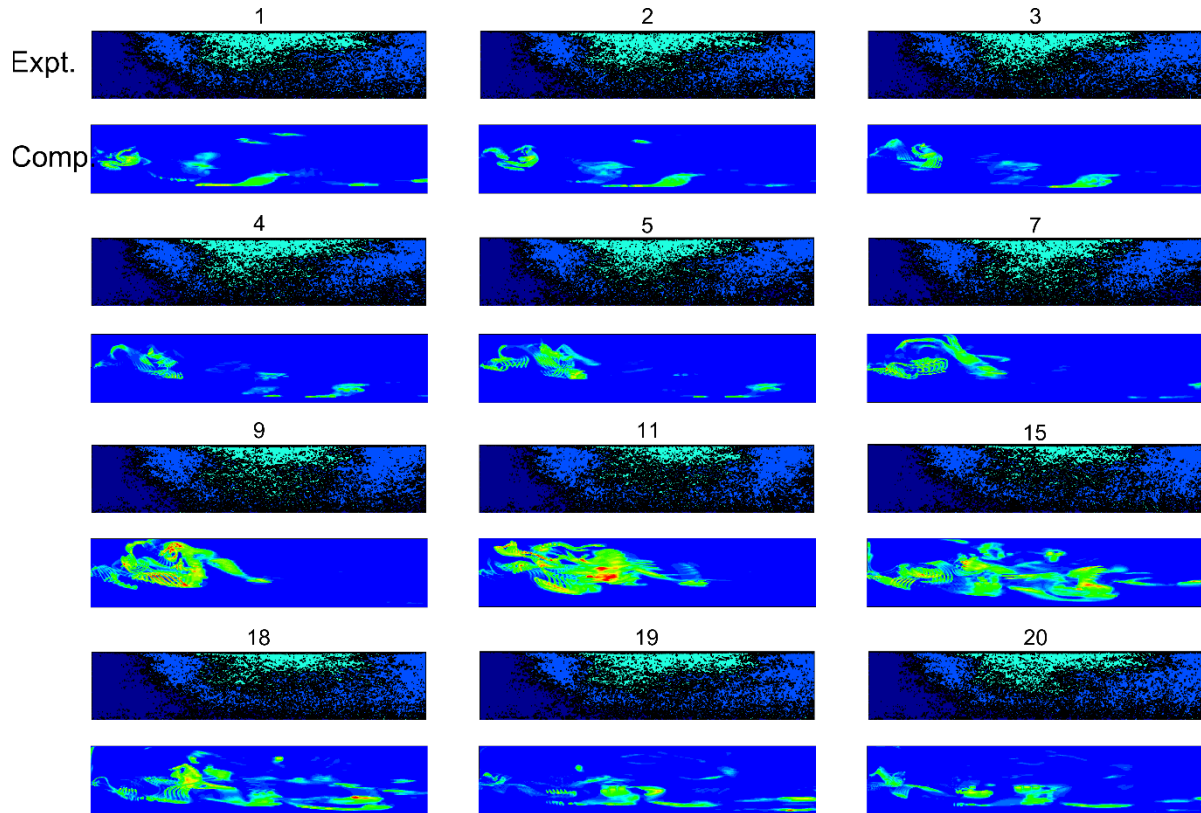
Figure 30: Comparison of selected inverse Abel transformed CH* radical images from the experiments and the computations.

A cycle representative of the limit cycle behavior is shown in Figure 31. Corresponding details of the flow-field at the first point of the cycle are shown in Figure 32. Pressure fluctuations in this case remain moderate, which can be seen at the start of the cycle. The lower pressure amplitude in this case can be attributed to the spread of the fuel consumption along the axial direction. This is consistently predicted by both the chemical kinetics mechanisms.

(a) Global-1   (b) GRI-1.2
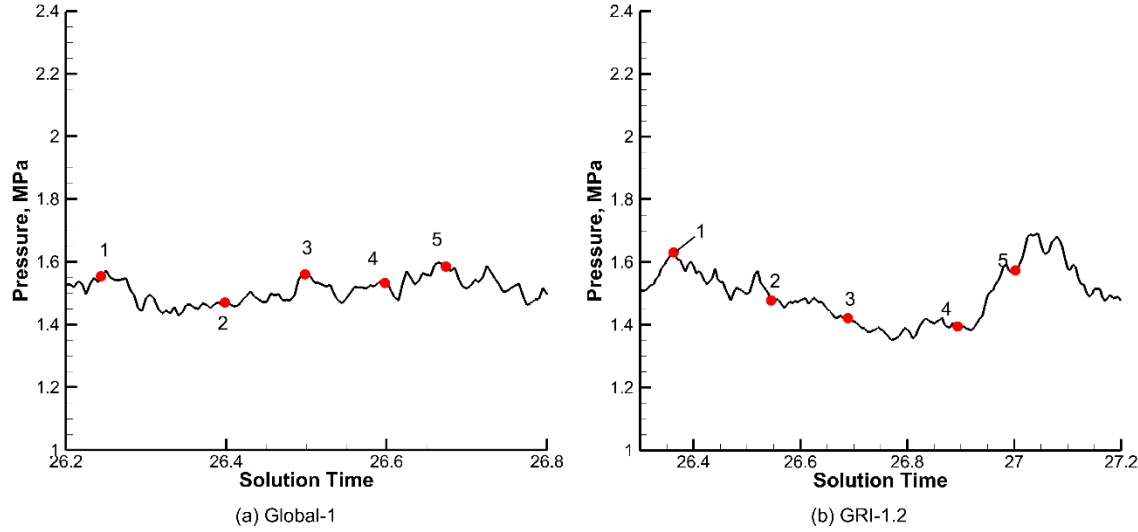
*Figure 31: Pressure cycle chosen for detailed analysis of the oxidizer post length 8.89 cm.*
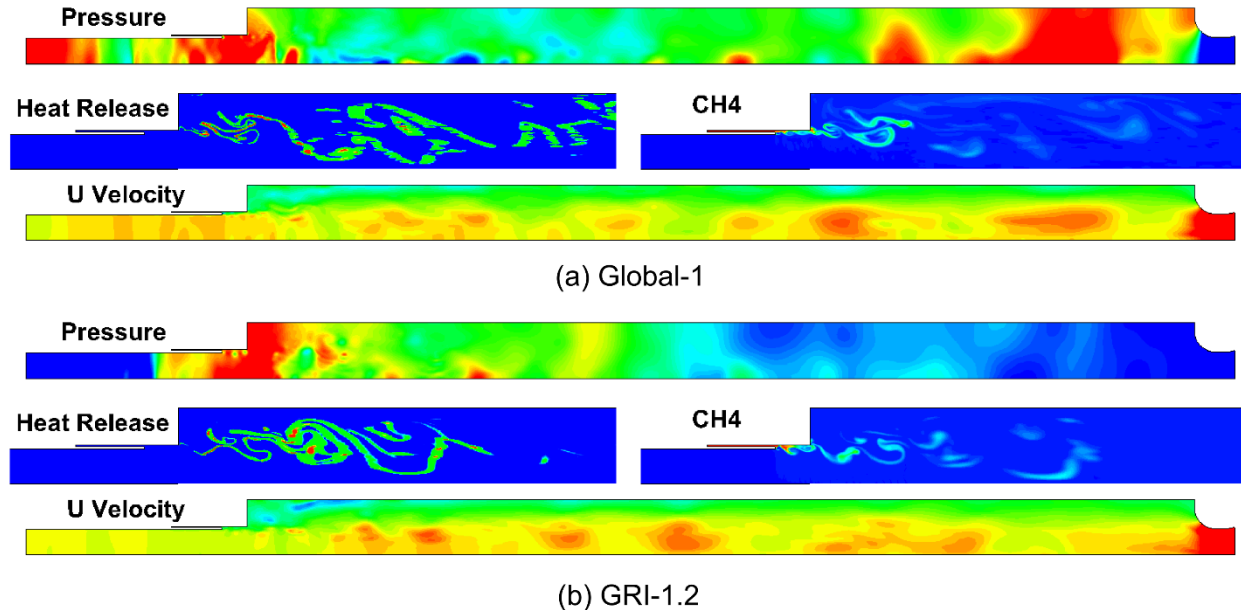

(a) Global-1

(b) GRI-1.2

Figure 32: Limit cycle analysis: time-1 for oxidizer post length of 8.89 cm. The scales are - pressure: 1.4 to 1.6 MPa; heat release: 0.01TW/m3 to 1TW/m^3; fuel mass fraction: 0 to 1 and velocity: -200 to 400 m/s.
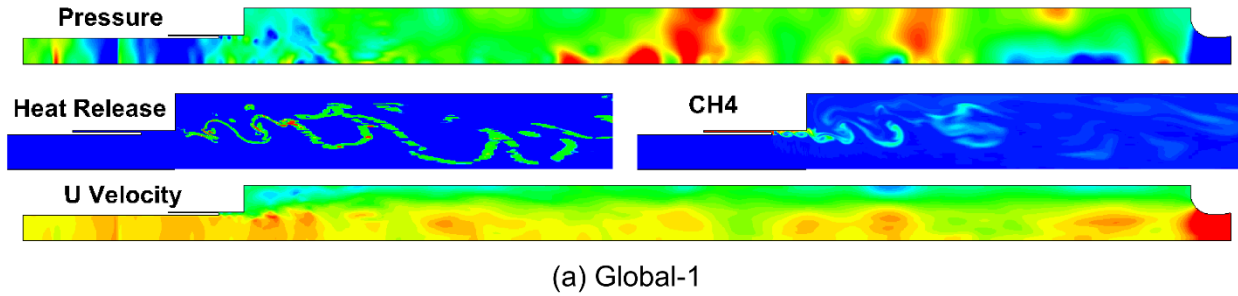
(a) Global-1
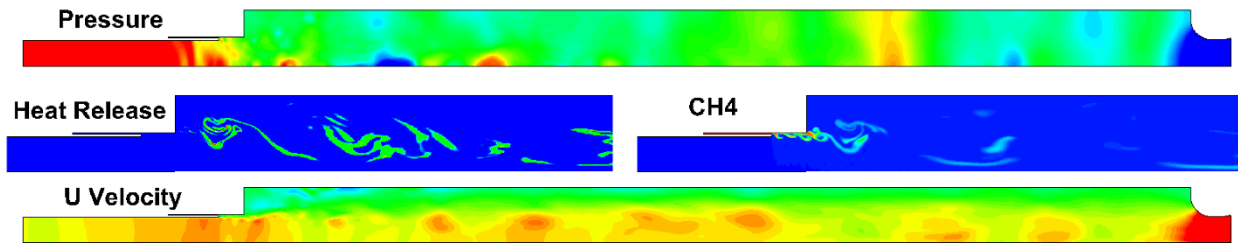
(b) GRI-1.2

Figure 33: Cycle point – 2, oxidizer post length of 8.89 cm.

At time 2 of the cycle, shown in Figure 33, the reflected pressure wave from the oxidizer post arrives at the dump plane of the combustor, which is earlier than the previous case. The pressure wave in the combustor has not yet reached the downstream boundary. The increased velocity as the pressure wave exits the oxidizer post induces better mixing in the shear layer. Compared to time 1, the heat release does not diminish significantly. It is noteworthy that the uninterrupted consumption of fuel signifies hot products moving at higher velocities through the combustor, therefore aiding the mixing and distributing the heat release in the combustor.
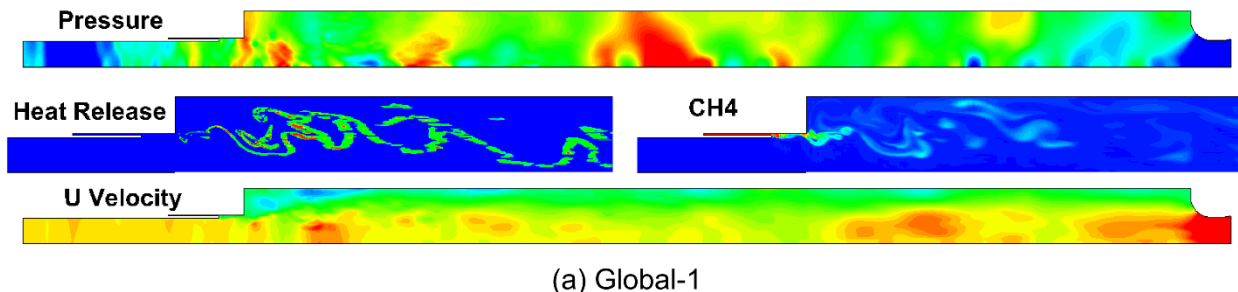
(a) Global-1
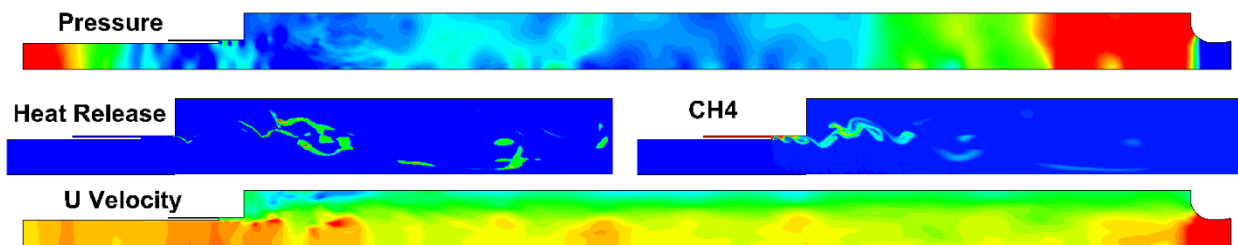
(b) GRI-1.2

Figure 34: Cycle point – 3, oxidizer post length of 8.89 cm.

At time 3 of the cycle, shown in Figure 34, the fuel consumption near the back step is reduced. However, a favorable pressure gradient during the previous step continues to drive the high velocity near the dump plane, favoring mixing within the shear layer and ingestion of the hot products from the corner recirculation zone. This phenomenon is more prominent in the detailed kinetics predictions. Due to near continuous heat release in the case of global-1

mechanism, pressure near the head end of the combustor remains relatively high. Consequently the shear set up due to oxidizer velocity near the dump plane is less, which in turn affects the fuel consumption.

The flow field at time 4 of the cycle is shown in Figure 35. There is increased heat release prior to the arrival of the reflected pressure wave in the combustor but the heat release is axially distributed unlike the unstable case, thus limiting the pressure rise during the up cycle. The last snapshot in Figure 36 shows heat release occurring throughout the domain, while fuel consumption is distributed in isolated pockets enveloped in accelerating hot products. The gradual fuel consumption can also be deduced from peak heat release rate, which in this case is neither as organized nor as strong as the previously discussed unstable case.

(a) Global-1

(b) GRI-1.2
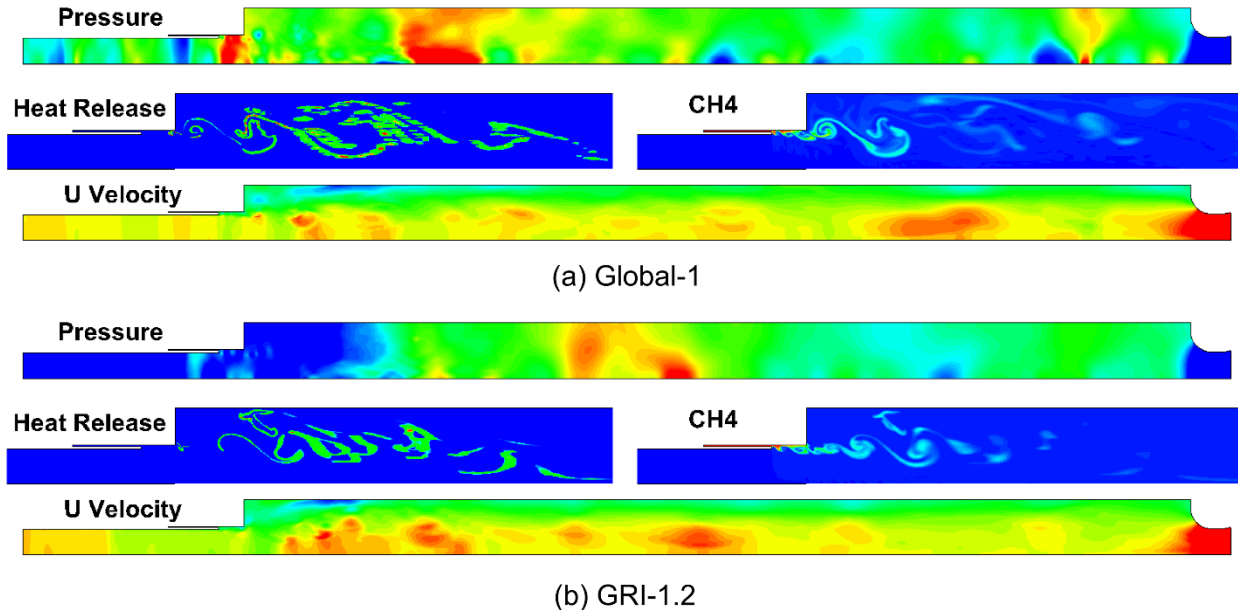
Figure 35: Cycle point – 4, oxidizer post length of 8.89 cm.

Primarily, the predictions of the two chemical kinetics schemes are not as distinct in this case as the previously described unstable case. The reason for this contrast is the underlying continuous processes of mixing, hot gas ingestion in the shear layer and combustion in an elongated reaction zone. Albeit the similarities in the contours, a prominent distinction between the two mechanisms in this case is the smooth heat release rate in the case of GRI-1.2. In the case of global-1 mechanism, final products separate the reactants immediately, preventing further mixing. This leads to streaks of unreacted propellants in the combustor as opposed to pockets of fuel seen on the fringes of the reaction zone in the case of GRI-1.2 predictions.

(a) Global-1

(b) GRI-1.2
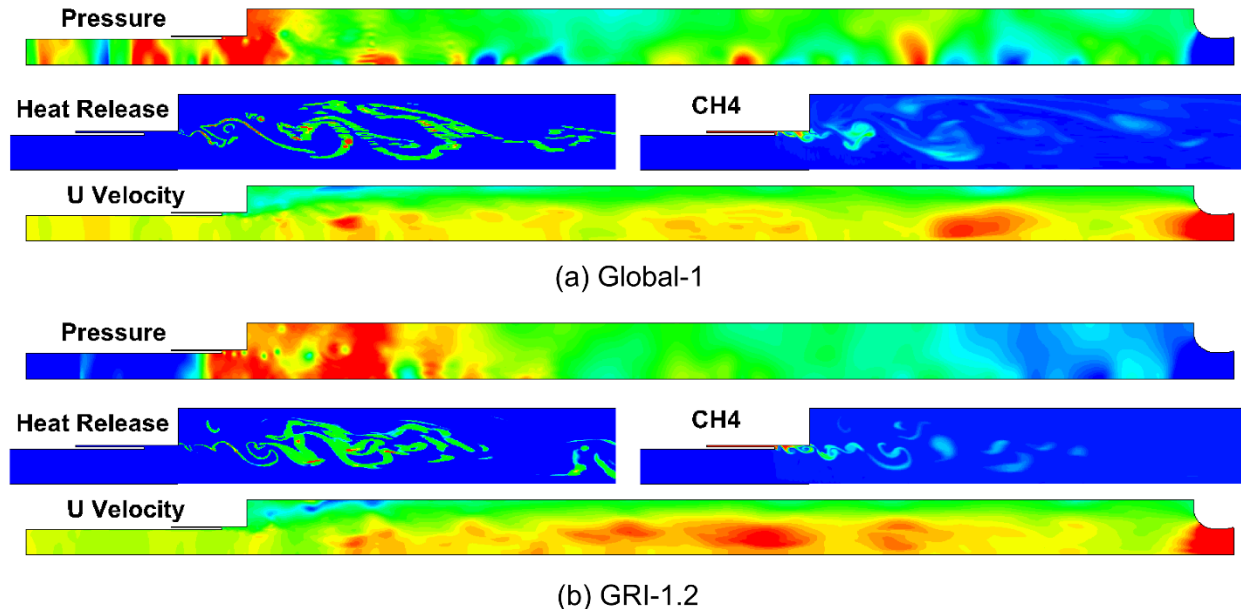
Figure 36: Cycle point – 5, oxidizer post length of 8.89 cm.

Figure 37 shows the shear layer and standard deviation of equivalence ratio within the shear layer in the case of the shorter oxidizer post length. The shear layer clearly shows hot gas ingestion close to the dump plane, which promotes the pre-ignition reactions, allowing earlier heat release in comparison to the previous case. It shows limited variation, supporting the hypothesis of continuous processes. The importance of mixing in the oxidizer post and the shear layer close to the dump plane can be affirmed from this trend.

(a) Shear layer sized by equivalence ratio (0.1 - 3.5) and colored by temperature of the mixture.

(b) Fluctuations in the standard deviation of the shear layer equivalence ratio.
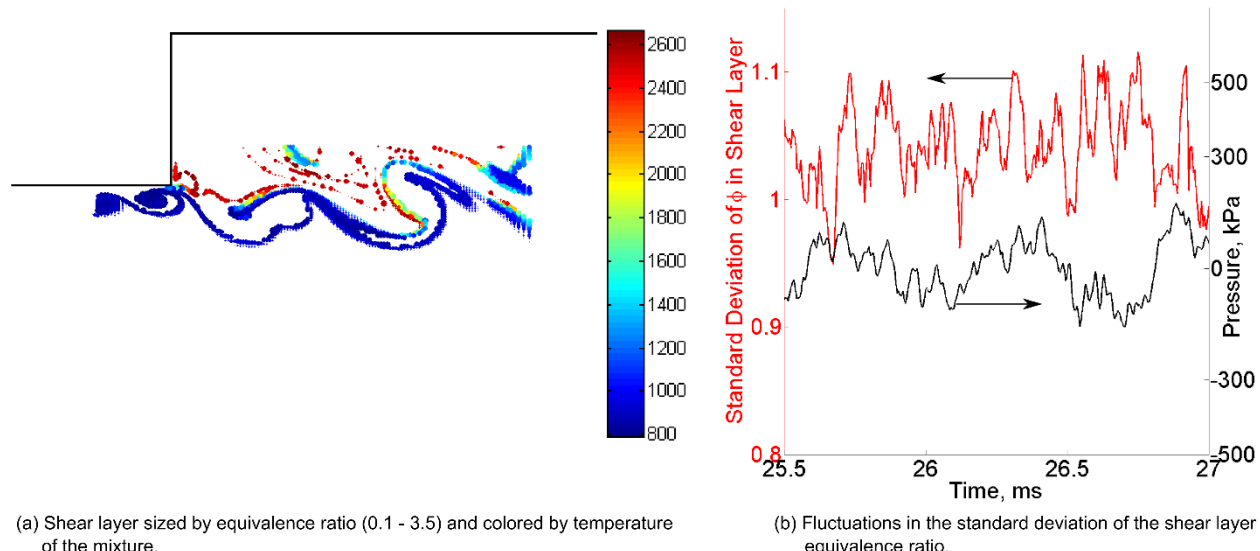
Figure 37: Shear layer unmixedness variation with pressure for the oxidizer post length 8.89 cm case. Predictions with GRI-1.2 kinetics.

Unstable Operating Condition - Long Length

In the CVRC experiment, both stable and unstable operation can be found for the long oxidizer post length. Taking advantage of continuous variability, this oxidizer post length has been approached from both longer and shorter lengths to avoid any historic effects. It was found to be on the cusp of stability, with some experiments showing stable and others showing unstable behavior. In computations, both axisymmetric two-dimensional as well as three-dimensional simulations with global kinetics have predicted unstable operation of the CVRC at the oxidizer post

length of 19.05 cm [18]. Simulations with GRI-1.2 also predict an unstable mode of the CVRC at the longer oxidizer post length. This is possibly due to the assumption of adiabatic wall boundary condition in the simulation whereas in the experiments, partial or complete wall section can transfer the incident heat out of the combustor. Although a complete picture of this transient phenomenon has been illusive, some insight can be obtained by following the cyclic flow field predicted with detailed kinetics.

A representative pressure cycle is shown in Figure 38. As with the previous cases, the detailed kinetics predictions present a steeper pressure rise followed by gradual decay. The small pressure rise near the bottom of the cycle that is commented upon in the previous section is also present in this case. It is however, shifted towards the beginning of the pressure rise in the cycle. This is expected with the longer oxidizer post length since it is due to arrival of reflected pressure wave in the oxidizer post to the dump plane.

The flow field at the first point in the cycle is shown in Figure 39. Although the overall cycle bears resemblance to the one described for the unstable case, there is a difference in the mechanism of instability for the longer oxidizer post length. At time 1, the initial high pressure wave is generated by the rapid fuel consumption and heat release. The upstream traveling wave causes the fuel to move radially inward, constituting a cross flow in the high speed oxidizer stream. It should be recognized that such an obstruction of the oxidizer flow due to axisymmetric assumption is unrealistic and will not occur in 3-D simulations. In this case, it marks the separation between the fuel consumption and accumulation events.

At time 2 of the cycle, shown in Figure 40, the fuel accumulation and reduced heat release close to the back step of the combustor is visible. At the same time, the pressure at the combustor head end is lower than the downstream end of the upstream traveling pressure wave. This favorable pressure gradient leads to an increase in the axial velocity at the dump plane. This increase in axial velocity drives the roll-up of the shear layer close to the back step, visible at time 3, shown in Figure 41. Relatively less mixed fuel and oxidizer form the two vortices similar to those seen in case of the oxidizer post length of 13.97 cm. Due to the increased oxidizer post length, the returning wave from the oxidizer post has yet to reach the fuel sleeve exit. At the next point of the cycle (time 4; Figure 42), the high velocity region near the fuel injector indicates the return of pressure wave from the oxidizer post. In contrast to the 13.97 cm case, where mixing is driven by the returning oxidizer post pressure wave, shear layer roll-up and the high-velocity oxidizer stream lead to earlier mixing of the reactants and combustion products. The heat release in this case happens before the returning wave in the oxidizer post reaches the head end of the combustor. The difference in the heat release locations between the two cases is due to this behavior. Since mixing and heat release occur earlier than the arrival of the reflected pressure wave in the combustor, the coupling of the acoustic mode and heat release mode is weaker. This uncertain coupling can explain the borderline stability in the case of longer oxidizer post length.

(a) Global-1   (b) GRI-1.2
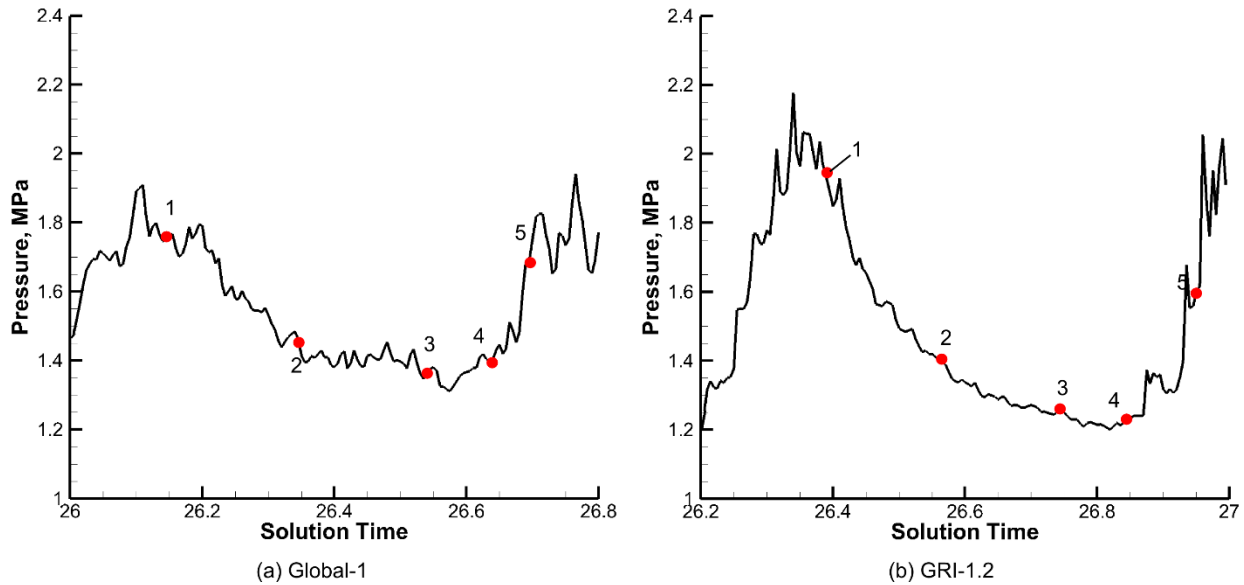
Figure 38: Pressure cycle chosen for detailed analysis of the oxidizer post length 19.05 cm.

(a) Global-1

(b) GRI-1.2
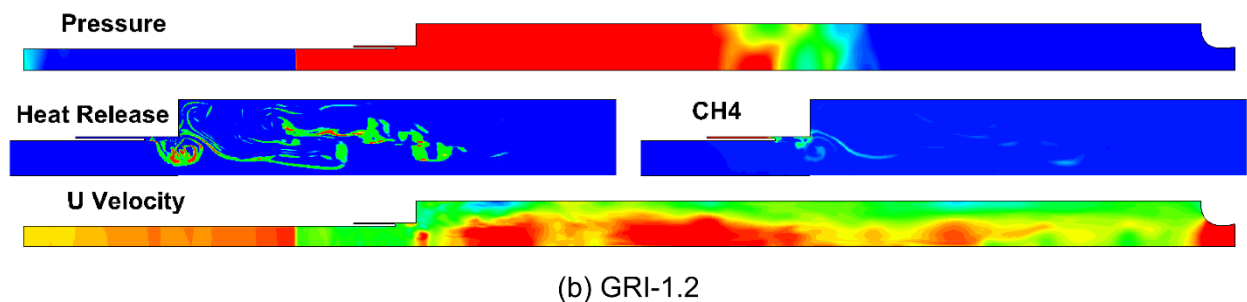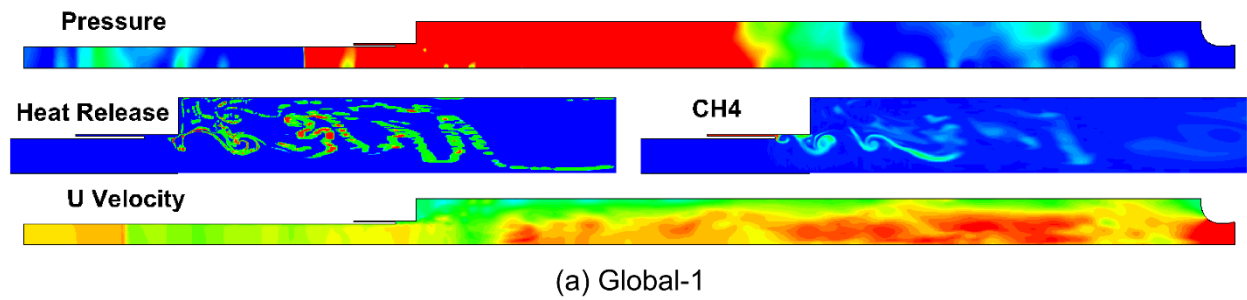
Figure 39: Limit cycle analysis: time-1 for oxidizer post length of 19.05 cm. The scales are - pressure: 1.4 to 1.6 MPa; heat release: 0.01TW/m3 to 1TW/m^3; fuel mass fraction: 0 to 1 and velocity: -200 to 400 m/s.

(a) Global-1

(b) GRI-1.2
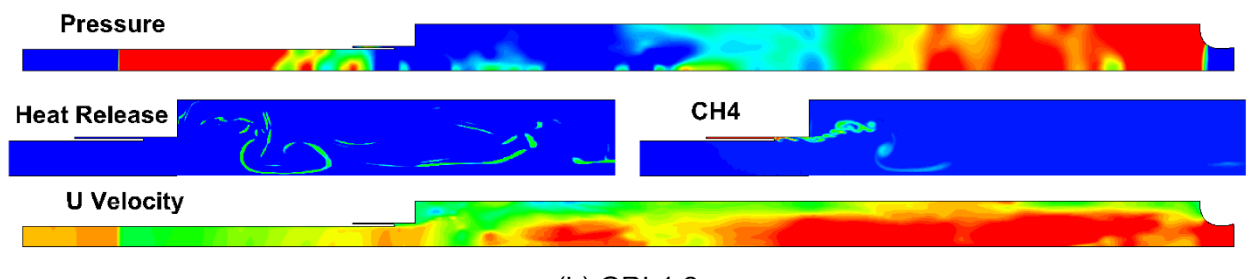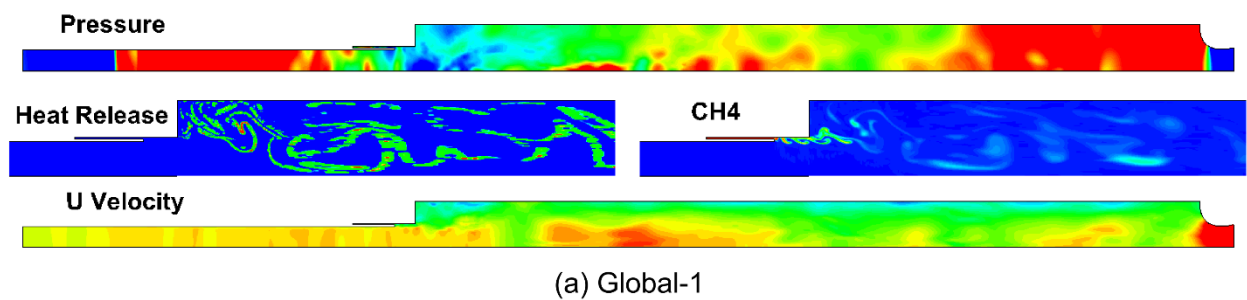
Figure 40: Cycle point – 2, oxidizer post length of 19.05 cm.

(a) Global-1

(b) GRI-1.2
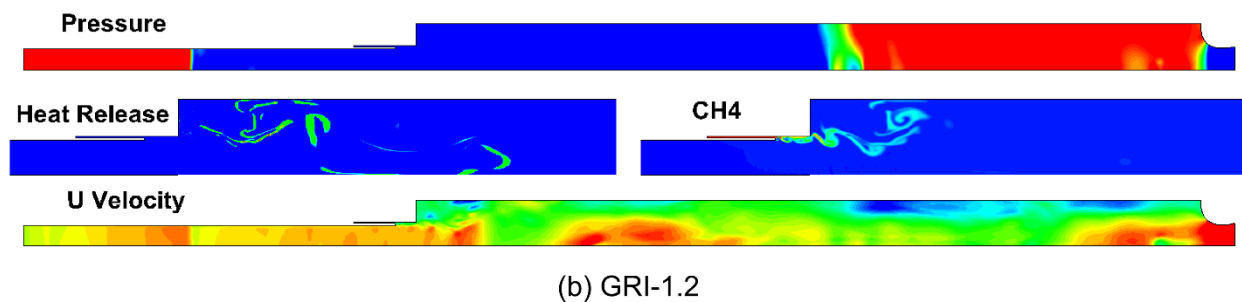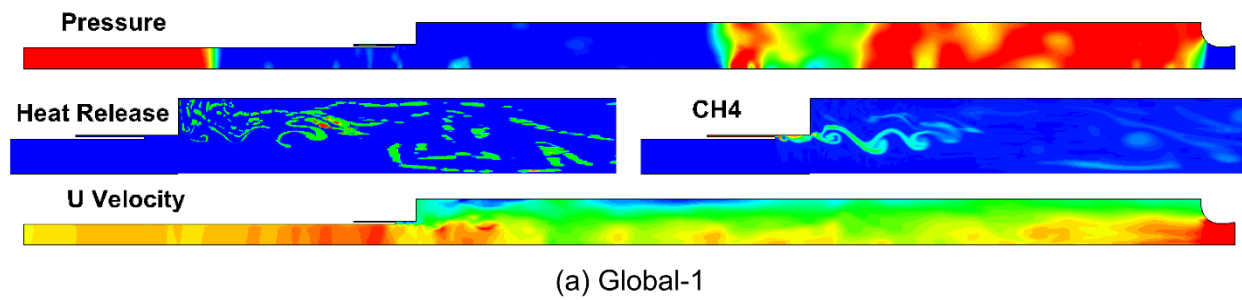
Figure 41: Cycle point – 3, oxidizer post length of 19.05 cm.

(a) Global-1

(b) GRI-1.2
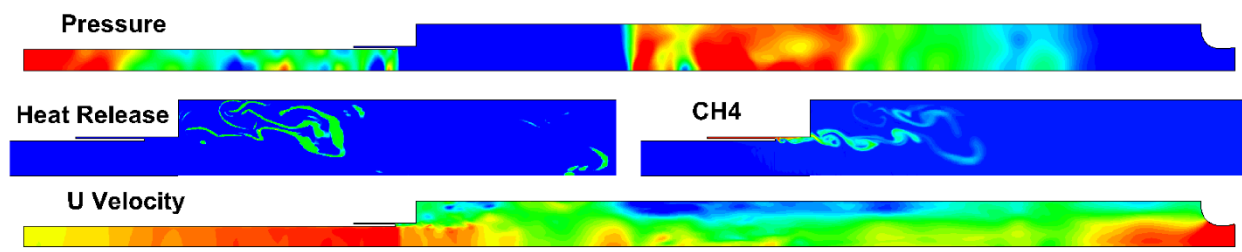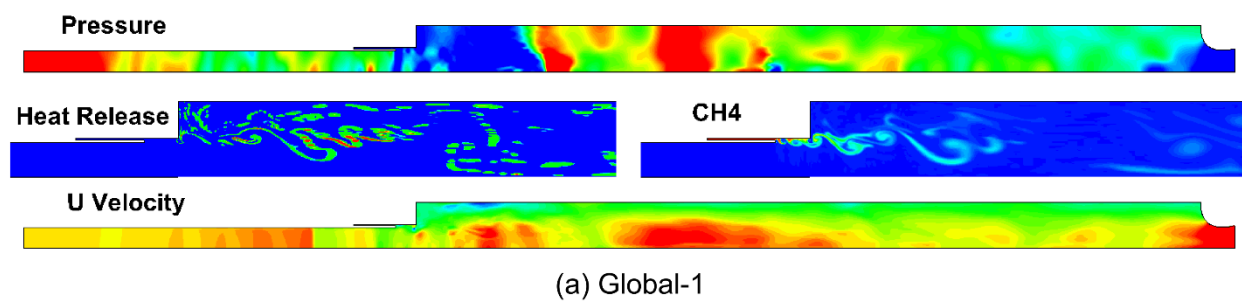
Figure 42: Cycle point – 4, oxidizer post length of 19.05 cm.

(a) Global-1

(b) GRI-1.2
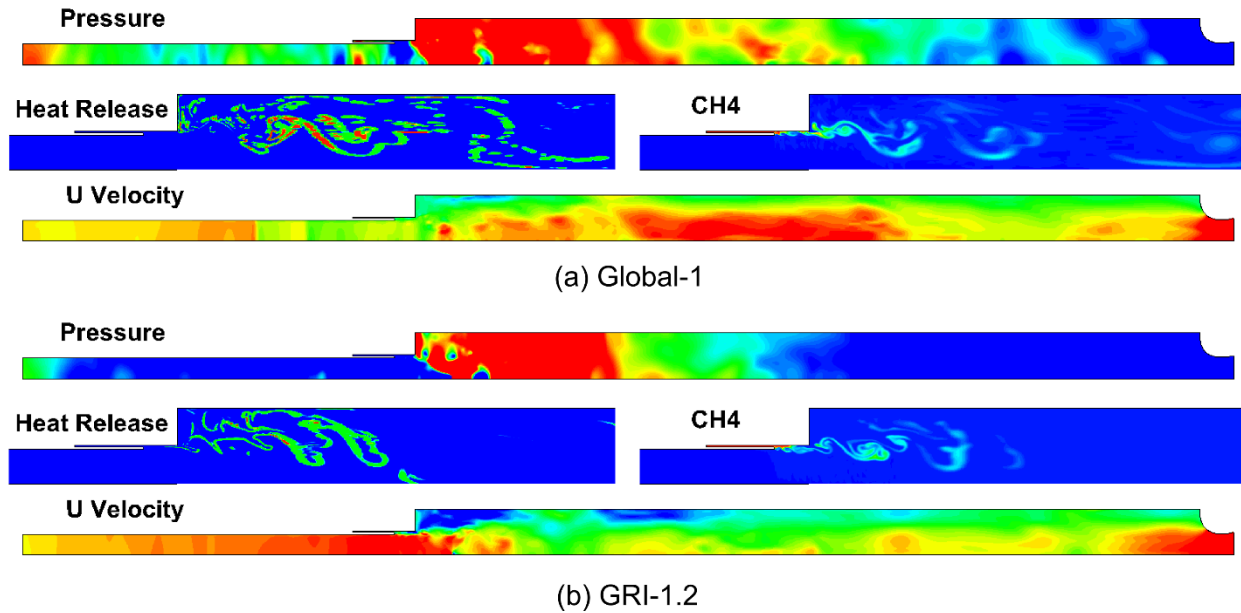
Figure 43: Cycle point – 5, oxidizer post length of 19.05 cm.

Figure 44 shows the history of equivalence ratio variation in the shear layer for the longer oxidizer post. It shows the first dip in the standard deviation due to the upstream moving pressure wave passing the fuel sleeve. A sharp second dip in the variation is observed subsequently, which suggests the role of the high velocity region formed near the fuel injector due to lower pressure at the combustor head end. Subsequent fuel accumulation and the cycle follows in the same manner as discussed before.
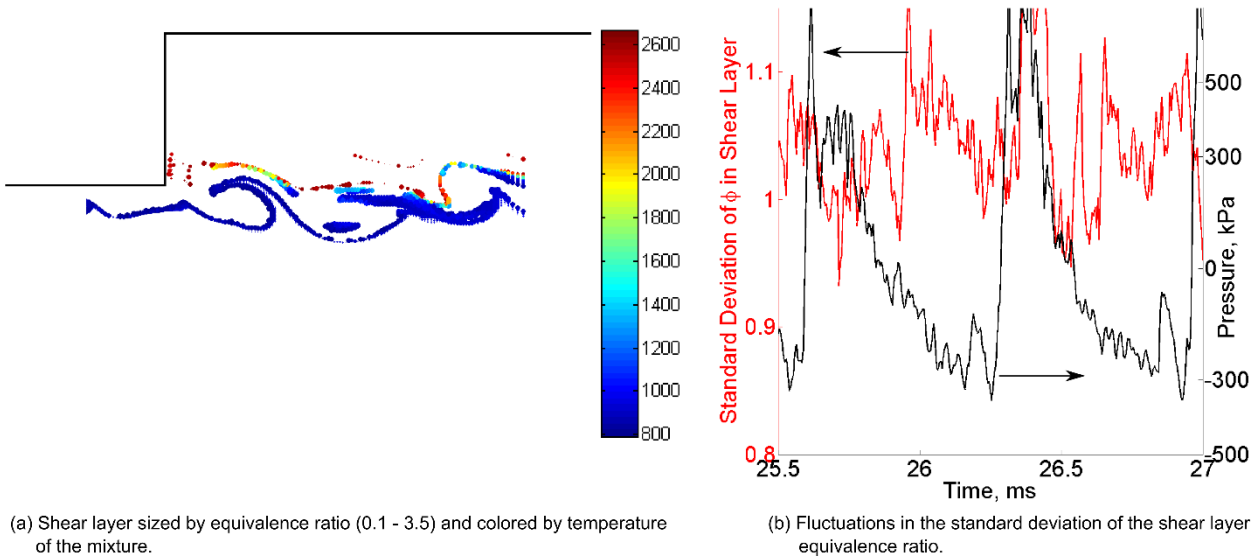
(a) Shear layer sized by equivalence ratio (0.1 - 3.5) and colored by temperature of the mixture.

(b) Fluctuations in the standard deviation of the shear layer equivalence ratio.

Figure 44: Shear layer history in the oxidizer post 19.05 cm} case, showing the early mixing due to increased oxidizer post length.

Simulations – Summary and Future Work

Characteristics of chemical kinetics schemes such as the ignition delay, temperature rise and heat release rate can impact the reacting flow simulations significantly. This effect is particularly important for modeling of the combustion instability in the CVRC experiments. Although the single step kinetics scheme predicts the self-excited combustion instability, predicted frequencies exceed the observations while the amplitude of the instability is lower.

The difference is more pronounced for high order harmonics where the detailed mechanism does a better job of capturing the harmonics compared to the global mechanisms.

Predictions of ignition delay, temperature rise and heat release rate with the detailed mechanism - GRI-1.2 are close to that of GRI-3.0 mechanism. The use of this detailed kinetics mechanism benefits the combustion instability predictions for the CVRC experiment. The use of GRI-1.2 mechanism also enables a direct comparison with the visual measurements, which is advantageous for the transient phenomena such as combustion instability.

Simulation of the short oxidizer post length shows axially extended fuel consumption due to less traverse time for the pressure wave in the oxidizer post. Mixing in the shear layer does not deviate significantly within the cycle. For the unstable oxidizer post length of 13.97 cm, mixing within the shear layer is related to the reflected pressure wave in the oxidizer post. Formation of an upstream moving vortex acts as a precursor to the coherent heat release that occurs upon return of the pressure wave in the combustor. Similar behavior is seen for the longer oxidizer post length, but an alternative mixing mechanism is seen due to increased axial velocity near the dump plane of the combustor.

Prior simulations of CVRC have shown the marked advantage of three-dimensional simulations over two-dimensional axisymmetric models. Unrealistic oxidizer stream contraction and separation of fuel and oxidizer due to product formation are some of the disadvantages that can be eliminated in three-dimensional simulations. The computational cost of three-dimensional simulations is at least an order of magnitude higher than the axisymmetric simulations. Also of interest is the use of accurate thermal boundary condition for the combustor wall. Further, the incorporation of appropriate turbulent combustion closure may also impact the accuracy of the combustion response. The above aspects will form the basis of continued and future research investigations.

Comparison between Experiment and Simulation

Computational models have the advantage that flow field data can be extracted from any of the cells in the computational mesh, whereas experimental measurements are limited in their spatial and temporal resolution. In the case of experimental light emission measurements, spatial resolution is limited by the line-of-sight integrated nature of the emission collection. Optical point measurements with spatial resolution comparable to the computational model used in this study have been demonstrated using a Cassegrain telescope arrangement [14], however, a small probe volume also significantly reduces the amplitude of the detectable signal thus making time resolved, or even phase-locked average measurements at high frequencies difficult. Line of sight integrated optical measurements sacrifice spatial resolution for improved signal amplitude and simplicity. It is important then when comparing line of sight integrated measurements from an optical probe to model data, that the model data is processed in a fashion representative of the experimental data collection. This processing allows for more direct comparisons between model data and experimental results.

Combustion heat release is a critical parameter involved in driving combustion instabilities in rocket combustors. Local heat release rate cannot be measured directly with non-intrusive instruments at time scales required to resolve high frequency heat release oscillations. The computational model in this study has the capability of predicting heat release with high spatial and temporal resolution, but there is no experimental measurement available to validate heat release predictions from the model. To provide direct comparison to experimental data, reaction steps were added to the chemical kinetics model that represent the production of radical species. Chemiluminescence measurements from the experiment, frequently assumed to indicate reaction heat release, can then be directly compared to the production of radical species in the computational model, and then compared to predicted heat release.

To extract model data that best represent experimental measurements, an understanding of the optical probe volume is required. The probe volume or field of view of the fiber optic probe used in this experiment is determined by the fiber diameter and the optic port geometry in the combustor chamber wall. A schematic of the probe installation is shown in Figure 45. The optic port in the chamber wall provides the limiting aperture in this case. The solid angle of the probe volume was calculated using ray transfer matrix analysis of the most extreme ray captured by the probe. The analysis accounted for apertures at the fiber face and in the optic port in the chamber wall, refraction through

the sapphire window at the bottom of the optic port, and relative distances of the components in the optic port. It was assumed that light transmitted to the fiber via reflections from hardware surfaces were negligible, no light was collected from within the optical port, refraction index gradients in the combustion gas were negligible, and that chemiluminescent emissions for the wavelengths under investigation were not reabsorbed by the combustion gas, that is to say the gas is optically thin. The validity of this final assumption was investigated in depth as reabsorption of the emission signal may significantly skew the comparability of model and experimental data. To represent this probe volume in the model data, the 2-D mesh was first revolved about its center axis transforming it into a 3-D axisymmetric grid. Cell centers on this grid that fell in the probe volume as discussed were isolated, and the relative amount of light collected from each was determined using the ray transfer matrix analysis technique. Assuming diffuse emission of light from the center of each cell, a factor was calculated for each cell that describes the fraction of diffuse light emission visible by the optical fiber. A cross section of the probe volume in the computational domain is shown in Figure 46 where the points representing the cell centers are colored by the fraction of diffusely emitted light collected by the optic probe. It should be noticed that a larger fraction of diffusely emitted light is collected nearest to the probe face, despite the smaller diameter of the probe volume, and this fraction quickly decreases toward the far end of the probe volume.
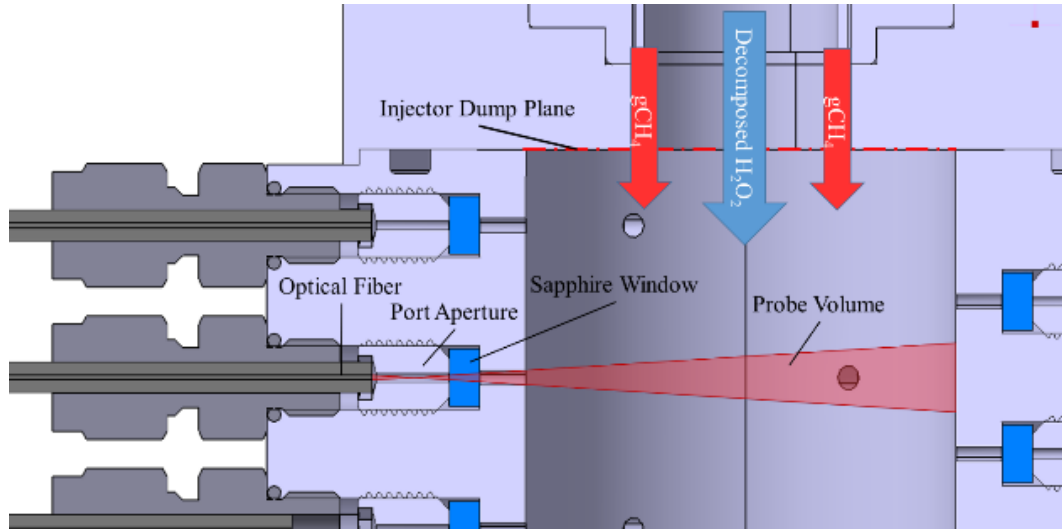
Figure 45: Optical probe configuration in combustor head end.
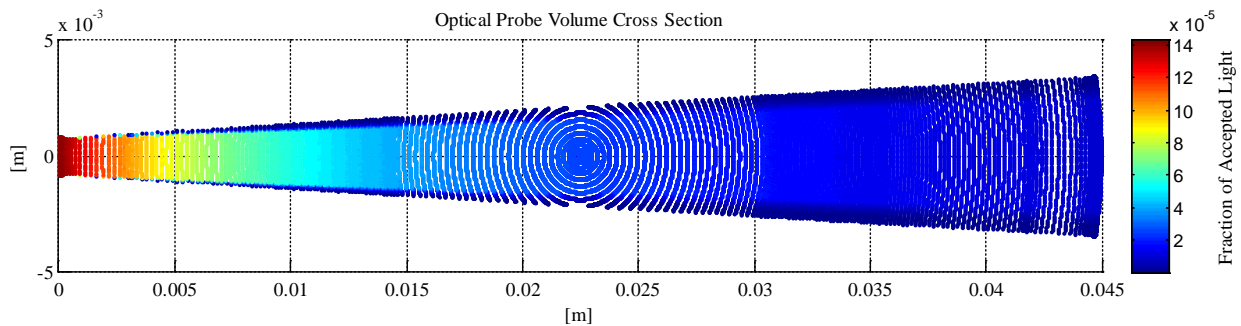
Figure 46: Cross section of optical probe volume colored by fraction of diffuse light collected from each cell based on ray transfer matrix analysis. Each data point represents the center of a cell in the revolved axisymmetric computational model. Variation in density of data points and circular groups of data points are caused by the revolution of the original 2-D axisymmetric mesh and cell density variation in the mesh. All data processing is performed on a volumetric basis to negate the effects of cell volume variation.

The assumption that the medium is optically thin is critical to the direct comparison of experimental and model data. Reabsorption of light emission in the combustion gas could significantly skew the line-of-sight integrated optical

measurements. An analysis of the optical depth of the combustion gas based on computational model data for species number density was performed to verify the optical thinness assumption.

When incident radiation interacts with matter, the radiation can undergo three basic physical processes: absorption, transmission and reflection: reflectivity (ρ) is defined as the fraction of light that undergoes reflection, absorptivity (α) is the fraction of light that is absorbed by the material, and transmissivity (τ) is the fraction of light that passes through the material unhindered. Equation $\rho+\alpha+\tau= 1$ (1 is derived from the principle of conservation of energy [2]:

$$\rho + \alpha + \tau = 1 \tag{1}$$

For the purpose of estimating the significance of optical absorption it may be assumed that individual molecules are strong absorbers. Additionally, gases have low density, thus it can be assumed that optical reflection is negligible in the combustion gas. In a high pressure system the density of potential absorbing molecules increases linearly with pressure, and so absorption effects can become significant.

Optical depth, or optical thickness is the natural logarithm of the fraction of light (transmittance) that is able to travel unhindered along a path. It gives an indication of how opaque a material is to the transmission of an electromagnetic wave. Optical depth is a dimensionless quantity and is given by Equation$T$=-ln$\left(\frac{I}{I_0}\right)$ = -ln(τ)

(2. T is the optical depth of the medium. I_0 corresponds to the irradiance of incident electromagnetic wave, and I is the irradiance of departing electromagnetic wave. τ is the transmissivity or spectral transmission.

$$T = -ln\left(\frac{I}{I_0}\right) = -ln(\tau) \tag{2}$$

The dominant OH* electronic transition is the $A^2\Sigma^+ \rightarrow X^2\Pi$ transition. The dominant CH* electronic transition is the $A^2\Delta \rightarrow X^2\Pi$. In both sets of transitions the (0,0) vibrational bands exhibit the strongest emissions [31]. In the process of combustion the photon energy of chemiluminescent OH* and CH* is congruent with an emission in the long wave ultraviolet (UV-A) spectrum. The wavelengths of the photons emitted by the dominant chemiluminescent line transitions of OH* and CH* occur at ~311.1nm and ~430.6nm respectively [13,31],.

Optical transmission occurs in a continuous spatial domain, but in this study the domain was discretized. To estimate the effects of reabsorption, or signal trapping, by the medium along the optic probe line of sight, the dataset captured by the probe volume was divided into layers along the probe's optical axis based on distance from the optic port entrance on the chamber wall. The solid angle fraction, species number density, temperature, and pressure data in each layer were averaged and collapsed into a single point ultimately producing a 1D data structure along the optical path. A sensitivity study suggested that 50 data points in the 1-D domain were required to minimize sample space error. Equation $I(z) = I_0 e^{-K_v g(v)z} = I_0\tau(v)$ (3 is referred to as the Beer-Lambert Law and is an inverse exponential power law representing the decay of an incident electromagnetic wave through an optical medium of a specified thickness. I_0 corresponds to the irradiance of the incident electromagnetic wave and I the irradiance of the departing electromagnetic wave. K_v is the absorption line strength at a given frequency, v. $g(v)$ is the normalized line shape function. The line shape function is based on the susceptibility to polarization at an absorption frequency of a medium for an incident wave frequency. τ is the transmissivity of the medium.

$$I(z) = I_0 e^{-K_v g(v)z} = I_0\tau(v) \tag{3}$$

The product of K_v and $g(v)$ is known as the attenuation or absorption coefficient. The line shape function generally follows the Voigt profile; a convolution of the Lorentzian and Gaussian profiles, which are attributed to collisional and Doppler line broadening respectively. For a continuum process the discretization of a continuous domain follows the model shown in Figure 47. The only parameters which need to be augmented for conversion to the discretized domain are the irradiance (I) and the optical path length (z), since the line strength and line shape are functions of optical frequency.
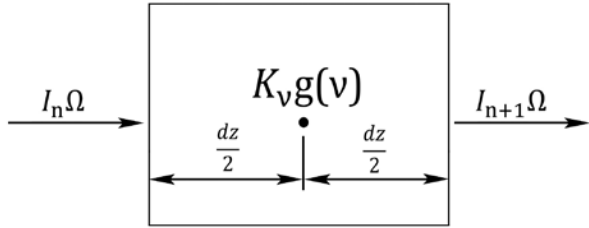
Figure 47: Representation of discretized domain for estimating absorption levels in the computational domain

In the case of chemiluminescent emission, the spectral profile is difficult to predict quantitatively. The bounds of the spectral behavior of a combustion system for a specific transition can be found using the maximum level of emission and maximum level of absorption for the particular wavelength.   The maximum level of absorption as a function of wavelength could then by characterized at single wavelengths representing the dominant transitions for OH* and CH*. The monochromatic emissions for OH* and CH* have the rotational line transitions $Q_1(13)$ and the $Q_{1c}(14)$ + $Q_{2c}(14)$ respectively [30]. Both transition sets occur within the Q-branch of the (0,0) vibrational band for each species. The CH* transition is actually two transition lines grouped together to form one transition line. This is because the spectral difference between the transition lines is negligible. Using monochromatic emission lines allows for prediction of the maximum amount of absorption that will occur at those wavelengths.

In the discrete computational domain, each point serves as an emission source and a potential sink, due to absorption. Dissipation of energy absorbed by ground state absorbing molecules is expected to occur rapidly, and so the ground state population remains large compared to population excited by absorption. Collisional quenching of excited species is also enhanced in a high pressure system. With high levels of absorption and quenching it is possible for the medium to reabsorb all of its emitted radiation becoming infinitely optically thick. Based on emission levels expected in combustion, the ability for each discrete point to absorb does not diminish over time.

Figure 48a represents the spatially averaged absorption fraction of OH* as experienced by the light collection probe during a large shift in pressure. The absorption level varies within one order of magnitude during the pressure oscillation. Similarly, Figure 48b represents the spatially averaged absorption fraction of CH* during the pressure shift. Though the levels of absorption for OH and CH differ by orders of magnitude, it is evident that the patterns of absorption differ between OH and CH during a cycle. Based on this result, it is concluded that the absorption effects are likely not consistent between different species for this case.

Figure 49a and 49b describe the time averaged absorption fraction of OH and CH as a function of optical distance from the measurement port. The absorption fraction is associated with the magnitude of the effect absorption has on the emission from each point in the discretized domain. Intuitively, absorption has the largest effect on emission from the point furthest from the collection probe entrance, that is on the opposite chamber wall. Similarly, absorption minimally affects emissions nearest to the collection probe entrance. The absorption fraction for both OH and CH does not exceed 1e-9. Therefore he maximum absorption levels of OH* and CH* reveal that there is a negligible level absorption within the system; thus the combustion domain can be considered optically thin for the OH* and CH* emissions of interest.

(a) OH*   (b) CH*
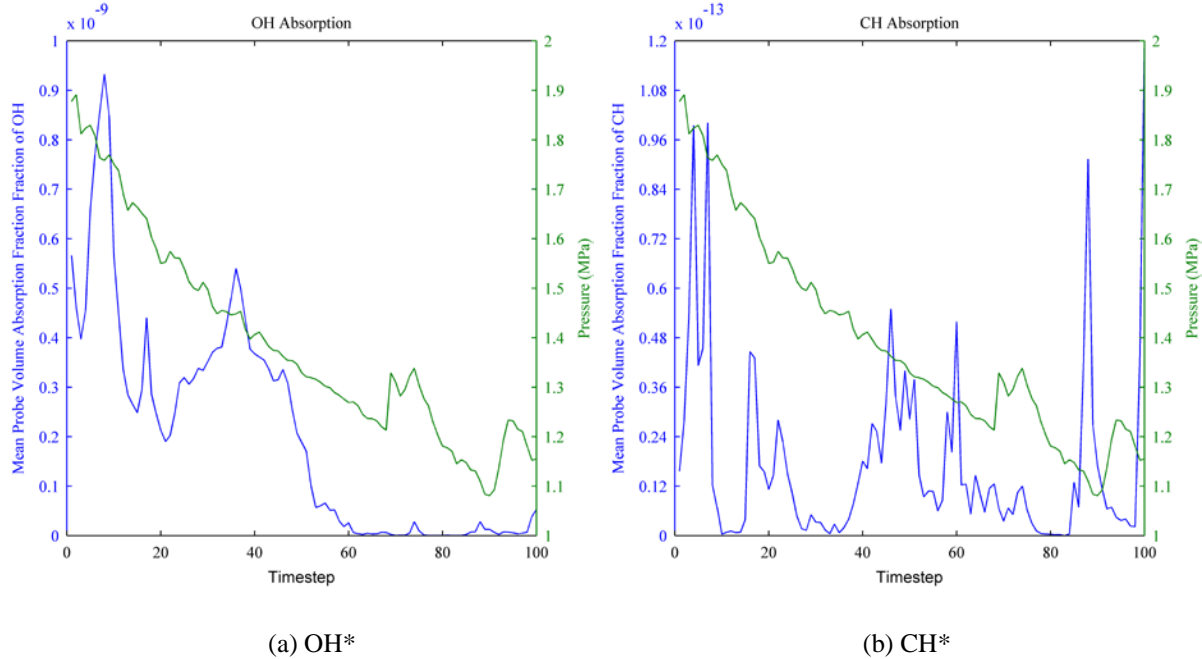
Figure 48: Average absorption of OH (a) and CH* (b) signal experienced by collection optics over 100 time steps of the computational model.*

(a) OH*   (b) CH*
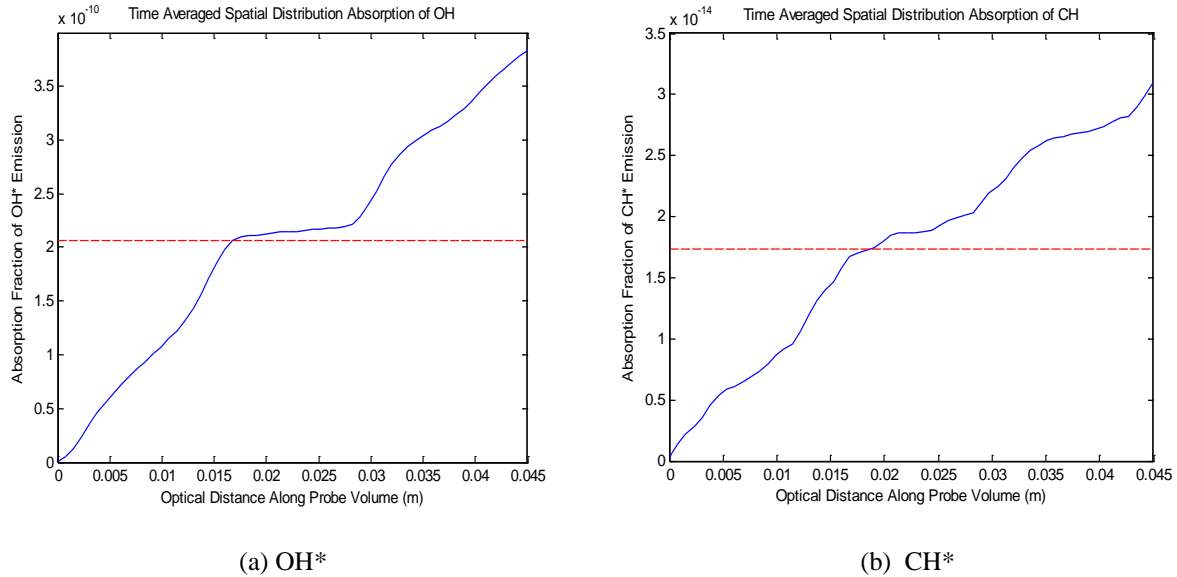
Figure 49: Effect of absorption as a function of distance from the collection optics for OH (a) and CH* (b) emissions*

Confirmation of optical thinness of the combustion allowed for extraction of model data of chemiluminescent photon production without corrections for reabsorption. Data for OH* and CH* photon emission was collected from the computational domain using the probe volume geometry discussed previously. Pressure and heat release data were also collected and averaged over the probe volume to enable a more direct comparison to the emission signals. Figure 50 shows the pressure fluctuation, OH* and CH* production rate, and heat release averaged over 37 pressure cycles based on the computation model described previously. This data suggests that OH* production correlates well with trends in pressure amplitude, but lags behind the peak heat release by nearly 40° in terms of pressure phase.
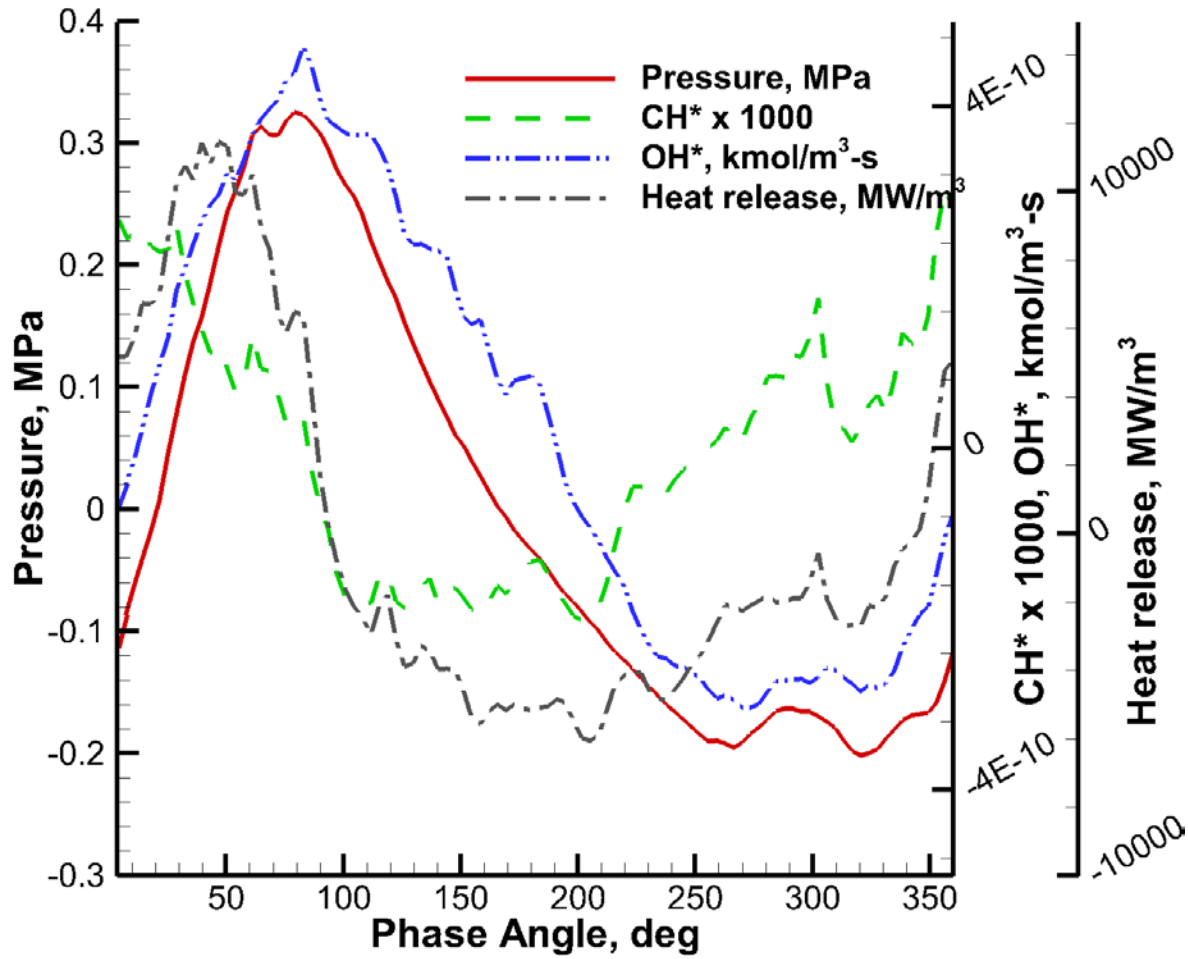
Figure 50: Phase averaged pressure heat release and radical species production rates measured from the computational model. OH* and CH* rates are determined by integrating throughout the probe volume with geometric weighting applied as discussed previously.

The variability from cycle to cycle due to randomness in the oscillating flow field makes comparison of phase averaged signals more meaningful than time resolved measurements. The phase averaged signals represent the most statistically significant behavior that is most common during each pressure oscillation period. The plots in Figure 51 compare pressure and light emission data from the experiment and computational model on a phase averaged basis. Phase averaged pressure signals shown in Figure 51a during limit cycle operation show excellent agreement between the experiment and model data. Average amplitudes are predicted with moderate accuracy for the duration of the pressure cycle. Figure 51b shows the comparison of phase averaged OH* emission intensity. This comparison reveals that although the general trend in OH* emission intensity is consistent between the model and experiment, the maximum emission intensity predicted by the model is out of phase with the signal measured in the experiment. The experimental measurement also shows an elevated level of OH* emission intensity during the pressure minimum near a phase angle of 300 degrees. This could be attributed with the long radiative lifetime of the OH* radical, and that it is likely to be produced by reactions occurring on the products side of the primary flame front. Figure 51c shows the comparison of phase averaged CH* emission intensity. Phase angles of peak values of CH* emission as predicted in the computational model agree well with experimental measurements. The measured CH* signal similarly appears to remain at elevated levels compared to the model during the pressure minimum. A secondary maximum occurs in the measured CH* signal at a phase angle of 200 degrees that is not predicted by the model and is not evident in the experimental or model data for the OH* emission. Figure 51d compares

chemiluminescent emission signals measured from the experiment to the predicted heat release fluctuation on a basis of pressure based phase averaging.

The model is able to predict the phase averaged pressure curve with moderate accuracy and, on this basis, the model heat release fluctuation and experimental emission measurements are compared directly, with the pressure curve providing the common link between model and experiment. This comparison shows that neither the OH* nor CH* signal measured in the experiment correlate in phase with the heat release fluctuation predicted by the model. The peak CH* emission from the experiment leads the predicted peak heat release by approximately 30° in terms of pressure phase angle while the peak OH* emission from the experiment follows predicted peak heat release by approximately 60°. Even though the model has captured with some level of accuracy compared to the experimental measurements the relative timing of chemiluminescent emissions from OH* and CH*, neither of these signals appear to be able to directly indicate heat release according to model predictions. Considering the turbulent nature of the reaction zone and line-of-sight integrated optical measurements there is evidence to suggest that chemiluminescent emission measurements acquired by the technique described here do have some potential to provide an estimate of spatio-temporal trends in heat release fluctuations, but their ability to provide a quantitative level of prediction is limited. This comparison suggests that perhaps a combination of OH* and CH* measurements may be most adequate in indicating at least the temporal trends for heat release in the particular case of this experiment.

a.) Phase averaged pressure
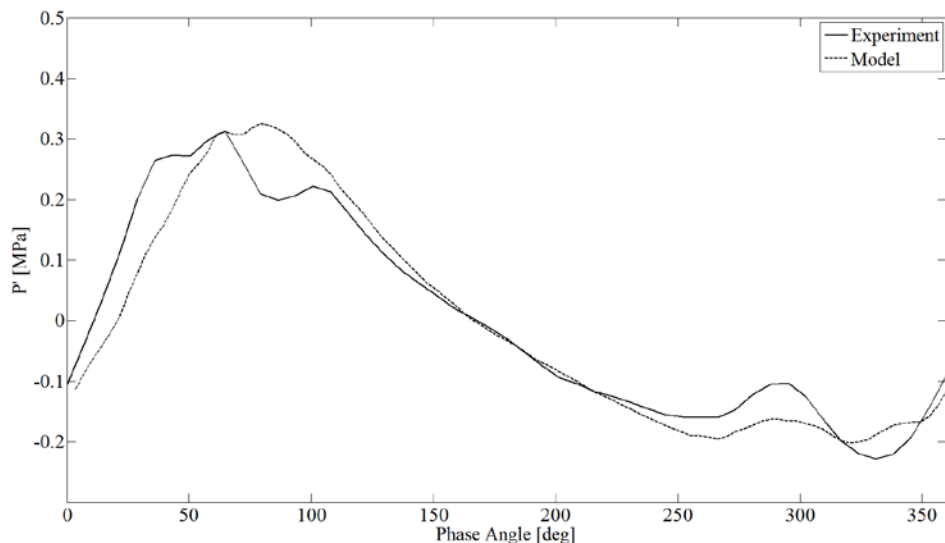
b.) Phase averaged OH* emission
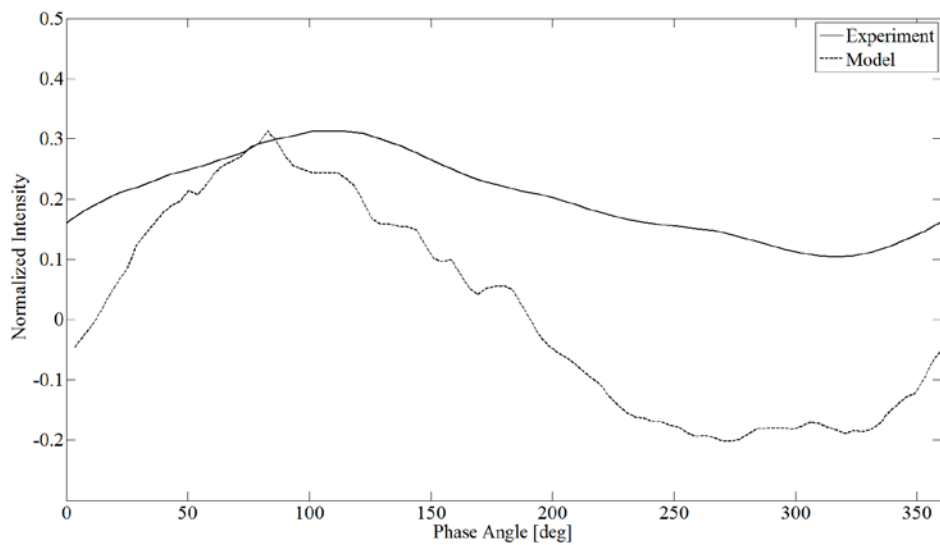
c.) Phase averaged CH* emission
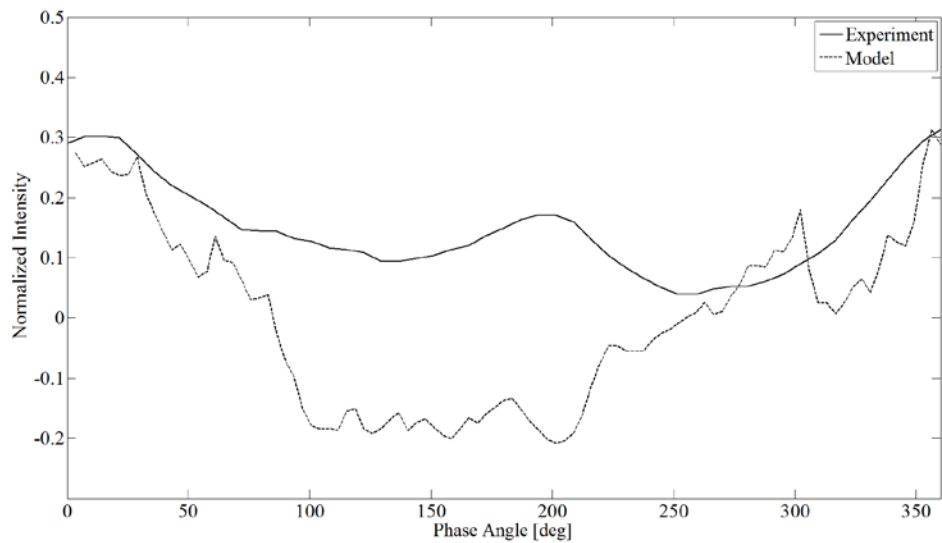
d.) Phase averaged OH* and CH* emission measurements versus predicted heat release
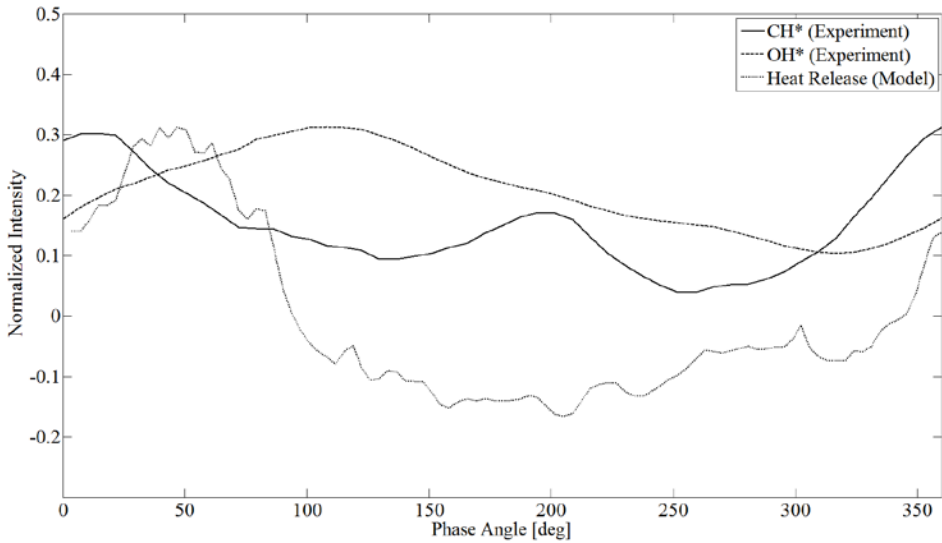
Figure 51: Comparison of computational model and experimental data phase averaged by the oscillating pressure signal. a.) Pressure b.) OH* emission c.) CH* emission d.) Experimental OH* and CH* emission and model heat release.

Conclusions and Recommended Future Work

Previous studies have shown that OH* and CH* emission intensity is a function of pressure, strain rate, equivalence ratio, and turbulence level. Since these flame properties have large variations at all times in the CVRC, it is difficult to decouple the chemiluminescent emission from all variables except heat release in experimental measurements. Emission due to chemiluminescence can, however, be isolated from other flame property variables in a computational model. The detailed kinetics model previously described is used to investigate the relationship between chemiluminescent species and heat release rate of the flame. This predicted relationship is then compared to experimental results both to check the validity of the model and to provide insight on the ability of the chemiluminescent light emission to indicate heat release in the unstable CVRC flame.

The average spectrum collected from CVRC combustion light emission indicates that optically band-pass filtered images of high pressure turbulent combustion may contain substantial emission from species that are not necessarily of interest. In the case of lean, high pressure, turbulent, non-premixed flames such as that of the CVRC, CO_2* chemiluminescence is dominant in the CH* emission band and also has a significant contribution in the OH* emission band. Low CH* emission intensity in the CVRC flame makes detection difficult, and measurements may not have the fidelity required for resolution of spatial and temporal distributions. Therefore, one must use caution in analyzing CH* or OH* chemiluminescence images under the assumption that they represent energy release as they are affected by emission from other species.

The detailed chemistry model was able to predict the strong OH* emission when compared to CH* emission intensity as observed in the experiment. Both experimental data and the detailed chemistry kinetics model indicate a phase difference in the line-of-sight integrated chemiluminescence measurements of OH* and CH* radical species at the location being investigated. Experimental phase averaged spectra indicate that the phase angle of peak CH* chemiluminescence is about 50 degrees ahead of the pressure peak, while the computational model predicts a phase lead of about 60 degrees. The phase angle of peak OH* chemiluminescence lags peak pressure by about 40 degrees as measured in the experiment, while in the computational model peak OH* chemiluminescence lags peak pressure by only about 7 degrees. Calculation of the radicals OH* and CH* from computations is based on the assumption of a quasi-steady state reaction. While this is expected to be accurate for CH*, it may not be perfect in the case of OH* due to possible thermal excitation path. A better way to compare OH* needs to assimilate the OH* mechanism in the detailed chemistry and model its transport. This modified approach is proposed for future computations.

Although heat release cannot be compared directly to chemiluminescence in the experiment, CFD model data reveal the spatial distribution of heat release production in the combustor. The model suggests a strong spatial correlation between heat release and production of OH* and CH*. Considering only the volume observable by the fiber optic probe in the experiment, maximum average heat release occurs in phase with maximum CH* chemiluminescence and out of phase with maximum OH* chemiluminescence. If CH* chemiluminescence is correlated with heat release in the flame, then the major heat release event leads the acoustic pressure peak. The CFD model suggests that the interaction is more complex. The flame front and heat release zone is intricate and shows significant variation in the radial and axial flow directions in the chamber. These effects cannot be observed in simple line-of-sight measurements commonly employed for observing high pressure turbulent flames. Motion of vortical flow structures associated with high heat release may change the phase relationship between heat release and observable pressure and chemiluminescence intensity changes.

Due to spatial and temporal variations in chemiluminescence and heat release that are indicated by the detailed chemistry model and measured experimentally, it is concluded that for high pressure turbulent diffusion jet flames as seen in the CVRC, line-of-sight integrated CH* and OH* chemiluminescence measurements are insufficient in providing spatial and temporal detail required to investigate the complex interaction of energy release and combustion chamber acoustics but can complement model predictions. Although chemiluminescence measurements do not allow for quantification of heat release, they do help to describe the flame behavior and its interactions with chamber acoustics on a qualitative level.

The question of how to test the ability of computational models to predict heat release remains open. Despite several striking similarities between experimental measurements and model predictions, chemiluminescence measurements by the technique used here cannot capture the level of detail required to compare quantitatively to model predictions, but can reveal combustion and fluid dynamic interactions on a larger scale. More sensitive optics such as photomultiplier tubes may be better suited for collecting emission signals at high repetition rates and may allow data to be captured at higher signal to noise ratios while increasing the measurement rate.

Spatially-resolved heat release is critical to validating high-fidelity simulations of combustion dynamics, but are extThis work uses ch. The detailed kinetics model previously described is used to investigate the relationship between chemiluminescent species and heat release rate of the flame. This predicted relationship is then compared to experimental results both to check the validity of the model and to provide insight on the ability of the chemiluminescent light emission to indicate heat release in the unstable CVRC flame.

The average spectrum collected from CVRC combustion light emission indicates that optically band-pass filtered images of high pressure turbulent combustion may contain substantial emission from species that are not necessarily of interest. In the case of lean, high pressure, turbulent, non-premixed flames such as that of the CVRC, CO_2^* chemiluminescence is dominant in the CH* emission band and also has a significant contribution in the OH* emission band. Low CH* emission intensity in the CVRC flame makes detection difficult, and measurements may not have the fidelity required for resolution of spatial and temporal distributions. Therefore, one must use caution in analyzing CH* or OH* chemiluminescence images under the assumption that they represent energy release as they are affected by emission from other species.

The detailed chemistry model was able to predict the strong OH* emission when compared to CH* emission intensity as observed in the experiment. Both experimental data and the detailed chemistry kinetics model indicate a phase difference in the line-of-sight integrated chemiluminescence measurements of OH* and CH* radical species at the location being investigated. Experimental phase averaged spectra indicate that the phase angle of peak CH* chemiluminescence is about 50 degrees ahead of the pressure peak, while the computational model predicts a phase lead of about 60 degrees. The phase angle of peak OH* chemiluminescence lags peak pressure by about 40 degrees as measured in the experiment, while in the computational model peak OH* chemiluminescence lags peak pressure by only about 7 degrees. Calculation of the radicals OH* and CH* from computations is based on the assumption of

a quasi-steady state reaction. While this is expected to be accurate for CH*, it may not be perfect in the case of OH* due to possible thermal excitation path. A better way to compare OH* needs to assimilate the OH* mechanism in the detailed chemistry and model its transport. This modified approach is proposed for future computations.

Although heat release cannot be compared directly to chemiluminescence in the experiment, CFD model data reveal the spatial distribution of heat release production in the combustor. The model suggests a strong spatial correlation between heat release and production of OH* and CH*. Considering only the volume observable by the fiber optic probe in the experiment, maximum average heat release occurs in phase with maximum CH* chemiluminescence and out of phase with maximum OH* chemiluminescence. If CH* chemiluminescence is correlated with heat release in the flame, then the major heat release event leads the acoustic pressure peak. The CFD model suggests that the interaction is more complex. The flame front and heat release zone is intricate and shows significant variation in the radial and axial flow directions in the chamber. These effects cannot be observed in simple line-of-sight measurements commonly employed for observing high pressure turbulent flames. Motion of vortical flow structures associated with high heat release may change the phase relationship between heat release and observable pressure and chemiluminescence intensity changes.

Due to spatial and temporal variations in chemiluminescence and heat release that are indicated by the detailed chemistry model and measured experimentally, it is concluded that for high pressure turbulent diffusion jet flames as seen in the CVRC, line-of-sight integrated CH* and OH* chemiluminescence measurements are insufficient in providing spatial and temporal detail required to investigate the complex interaction of energy release and combustion chamber acoustics but can complement model predictions. Although chemiluminescence measurements do not allow for quantification of heat release, they do help to describe the flame behavior and its interactions with chamber acoustics on a qualitative level.

The question of how to test the ability of computational models to predict heat release remains open. Despite several striking similarities between experimental measurements and model predictions, chemiluminescence measurements by the technique used here cannot capture the level of detail required to compare quantitatively to model predictions, but can reveal combustion and fluid dynamic interactions on a larger scale. More sensitive optics such as photomultiplier tubes may be better suited for collecting emission signals at high repetition rates and may allow data to be captured at higher signal to noise ratios while increasing the measurement rate.

1   Ayoola, B., Balachandran, R., Frank, J., Mastorakos, E., and Kaminski, C., "Spatially resolved heat release rate measurements in turbulent premixed flames," Combustion and Flame, Vol. 144, 2006, pp. 1–16.

2   Bergman, et al., Fundamentals of Heat and Mass Transfer, 7th Ed., 2011, John Wiley and Sons.

3   Choi, Y., & Merkle, C. The Application of Preconditioning in Viscous Flows. *Journal of Computational Physics*, 207-223. 1993.

4   Elsamra, R. M., Vranckx, S., and Carl, S. A., "CH (A2Δ) Formation in Hydrocarbon Combustion: The Temperature Dependence of the Rate Constant of the Reaction C2H+ O2 CH (A2Δ)+ CO2," The Journal of Physical Chemistry A, Vol. 109, No. 45, 2005, pp. 10287–10293.

5   Farhat, S., Ng, W., and Zhang, Y., "Spatially resolved heat release rate measurements in turbulent premixed flames," Fuel, Vol. 84, 2005, pp. 1760–1767.

6   Feldman, T. W., Unstable combustion processes for a single element Shear/Coax injector in a longitudinal combustor, Master's thesis, Purdue University, 2013.

7   Fiala, T. and Sattelmayer, T., "On the Use of OH Radiation as a Marker for the Heat Release Rate in High-Pressure Hydrogen-Oxygen Liquid Rocket Combustion," 49th AIAA/ASME/SAE/ASEE Joint Propulsion Conference and Exhibit, 2013.

8   Frenklach, M., Wang, H., Goldenberg, M., Smith, G., Golden, D., Bowman, C., Hanson, R., Gardiner, W., and Lissianski, V., "GRI-Mech-1.2, An Optimized Detailed Chemical Reaction Mechanism for Methane Combustion," Tech. rep., Gas Research Institute, 1995.

9   Frenklach, M., Wang, H., Smith, G., Golden, D., Bowman, C., Hanson, R., Lissianski, V. *GRI-Mech-1.2, An Optimized Detailed Chemical Reaction Mechanism for Methane Combustion.* Gas Research Institute. 1995.

10   Garby, R., Selle, L., and Poinsot, T., "Analysis of the impact of heat losses on an unstable model rocket-engine combustor using Large-Eddy Simulation," 48th AIAA/ASME/SAE/ASEE Joint Propulsion Conference and Exhibit, American Institute of Aeronautics and Astronautics, 2012.

11   Garby, R., Selle, L., & Poinsot, T. Large-eddy Simulation of Combustion Instabilities in a Variable Length Combustor. *Comptes Rendus Mecanique*. 2013.

12   Gaydon, A. G. and Wolfhard, H. G., Flames: Their Structure, Radiation, and Temperature, Chapman & Hall Ltd., London, 1960.

13   Gaydon, A. G., The Spectroscopy of Flames, Chapman & Hall Ltd., London. 1957.

14   Haber, C., Vandsburger, U., Saunders, W., and Khanna, V., "An Experimental Examination of the Relationship between Chemiluminescent Light Emissions and Heat-Release Rate Under Non-Adiabatic Conditions," RTO AVT Symposium on Active Control Technology for Enhanced Performance Operational Capabilities of Military Aircraft, Land Vehicles and Sea Vehicles, May 2000.

15   Hardalupas, Y. and Orain, M., "Local measurements of the time-dependent heat release rate and equivalence ratio using chemiluminescent emission from a flame," Combustion and Flame, Vol. 139, 2004, pp. 188–207.

16   Harvasinzki, M., Huang, C., Sankaran, V., Merkle, C., Feldman, T., Anderson, W., and Talley, D., "Combustion Instability Mechanisms in a Pressure-coupled Gas-gas Coaxial Rocket Injector," 49th AIAA/ASME/SAE/ASEE Joint Propulsion Conference and Exhibit, American Institute of Aeronautics and Astronautics, July 2013.

17 Harvazinski, M. E., Modeling self-excited combustion instabilities using a combination of two- and three-dimensional simulations, Ph.D. thesis, Purdue University, 2012.

18 Harvazinski, M., Anderson, W., & Merkle, C. Analysis of Self-excited Combusion Instability Using Two and Three-dimensional Simulations. *Journal of Propulsion and Power*. 2013.

19 Harvazinski, M., Huang, C., Sankaran, V., Feldman, T., Anderson, W., Merkle, C., & Talley, D. Instability Mechanism in a Pressure-Coupled Gas-gas Coaxial Rocket Injector. *Joint Propulsion Conference and Exhibit* (pp. 1-21). San-Jose, CA: AIAA. 2013.

20 Higgins, B., McQuay, M., Lacas, F., Rolon, J., Darabiha, N., & Candel, S. Symmetric Measurements of OH* Chemiluminescence for Fuel Lean High Pressure Premixed Laminar Flames. *Fuel.* 2001.

21 Holton, M., Jackson, G., Gokulkrishnan, P., Klassen, M., & Roby, R. Autoignition Delay Time Measurements of Methane, Ethane and Propane Pure Fuels and Methane-based Fuel Blends. *Journal of Engineering for Gas Turbines and Power*. 2010.

22 Hornstein, B., Budnik, C., and Courtney, W., "Research Study of Light Emission Caused by Pressure Fluctuations in Rocket Engines," AFOSR Final Report No. 5520-F, 1966.

23 Hossain, A. and Nakamura, Y., "A numerical study on the ability to predict the heat release rate using CH* chemiluminescence in non-sooting counterflow diffusion flames," Combustion and flame, Vol. 161, No. 1, 2014, pp. 162–172.

24 Jones, W. and Lindstedt, R., "Global Reaction Schemes for Hydrocarbon Combustion," Combustion and Flame, Vol. 73, 1988, pp. 233–249.

25 Kathrotia, T., Riede, l. U., and Warnatz, J., "A Numerical Study on the Relation of OH*, CH*, and C2* Chemiluminescence and Heat Release," Proceedings of the European Combustion Meeting, 2009.

26 Kathrotia, T., Riedel, U., Seipel, A., and Moshammer, K., "Experimental and numerical study of chemi-luminescent species in low-pressure flames," Applied Physics B, Vol. 107, 2012, pp. 571–584.

27 Lauer, M. and Sattelmayer, T., "On the Adequacy of Chemiluminescence as a Measure for Heat Release in Turbulent Flames with Mixture Gradients," Journal of Engineering for Gas Turbines and Power, Vol. 132, No. 061502, 2010.

28 Li, D., Sankaran, V., Lindau, J., & Merkle, C. Computational Formulation for Multi-component and Multi-phase Flows. *43rd AIAA Aerospace Sciences Meeting and Exhibit, 2005*. AIAA. 2005.

29 Lian, C., Xia, G., & Merkle, C. Impact of Source Terms on Reliability of CFD Algorithms. *Computers and Fluids*, 1909-1922. 2010.

30 Lucht, R.P., Peterson, R.C., and Laurendau, N.M. Fundamentals of Absorption Spectroscopy for Selected Diatomic Flame Radicals. Purdue University Combustion Laboratory, Prepared for the National Science Foundation Grant ENG 75-03461, 86-89, 1978.

31 Luque, J., and Crosley, D.R., "Determination of the electronic transition moment and calculation of the transition probabilities in the electronic system (A-X) of OH and OD". J. Chem. Phys., 109, 439, 1998.

32 Najm, H., Paul, P., Mueller, C., and Wyckoff, P., "On the Adequacy of Certain Experimental Observables as Measurements of Flame Burning Rate," Combustion and Flame, Vol. 113, 1998, pp. 312–332.

33 Nori, V. N. and Seitzman, J. M., "Evaluation of Chemiluminescence as a Combustion Diagnostic under Varying Operating Conditions," 46th AIAA Aerospace Sciences Meeting and Exhibit, January 2008.

34 Nori, V. N. and Seitzman, J. M., "CH* chemiluminescence modeling for combustion diagnostics," Proceedings of the Combustion Institute, Vol. 32, No. 1, 2009, pp. 895–903.

35 Nori, V., & Seitzman, J. (2009). CH* Chemiluminescence Modeling for Combustion Diagnostics. *Proceedings of the Combustion Institute* (pp. 895-903). Combustion Institute.

36 Panoutsos, C., Hardalupas, Y., and A., T., "Numerical evaluation of equivalence ratio measurement using OH* and CH* chemiluminescence and non-premixed methane-air flames." Combustion and Flame, Vol. 156, 2009, pp. 273–291.

37 Price, R. B., Hurle, I. R., and Sugden, T. M., "Optical studies of the generation of noise in turbulent flames," Symposium on Combustion, Vol. 12, No. 1, 1969.

38 Rosen, S. C., Combustion instabilities in the transition region of an unstable model rocket combustor , Master's thesis, Purdue University, 2011.

39 Samaniego, J., Egolfopoulos, F., and Bowman, C., "CO2* Chemiluminescence in Premixed Flames," Combustion Science and Technology , Vol. 109, 1995, pp. 183–203.

40 Sandrowitz, A., Cooke, J., and N., G., "Flame Emission Spectroscopy for Equivalence Ratio Monitoring," Applied Spectroscopy, Vol. 52, No. 5, 1998, pp. 658–662.

41 Smith, R., Xia, G., Anderson, W., and Merkle, C., "Computational Studies of the Effects of Oxidizer Injector Length on Combustion Instability," 46th AIAA/ASME/SAE/ASEE Joint Propulsion Conference and Exhibit , American Institute of Aeronautics and Astronautics, 2010.

42 Smith, R., Xia, G., Anderson, W., and Merkle, C., "Computational Simulations of the Effect of Chamber Diameter on Single-Element Rocket Combustor Instability," 44th AIAA/ASME/SAE/ASEE Joint Propulsion Conference and Exhibit, 2008.

43 Smith, R., Xia, G., & Merkle, C. Computational Studies of the Effects of Oxidizer Injector Length on Combustion Instability. *46th AIAA/ASME/SAE/ASEE Joint Propulsion Conference and Exhibit.* AIAA. (2010).

44 Smith, R., Xia, G., Anderson, W., & Merkle, C. Computational Studies of the Effects of Oxidiser Injector Length on Combustion Instability. *Combustion Theory and Modeling*. 2012.

45 Srinivasan, S., Rajan, R., & Menon, S. (2014). Flame Dynamics During Combustion Instability in a High Pressure, Shear Coaxial Injector Combustor. *Flow Turbulence and Combustion*.

46 Sutton, G. P. and Biblarz, O., Rocket Propulsion Elements, John Wiley & Sons, New York, 7th ed., 2001.

47 Venkateswaran, S., Lindau, J., Kunz, R., & Merkle, C. Computation of Multiphase Mixture Flows with Compressibility Effects. *Journal of Computational Physics*, 54-77. 2003.

48 Walsh, K., Long, M., Tanoff, M., & Smooke, M. Experimental and Computational Study of CH, CH* and OH* in an Axisymmetric Laminar Diffusion Flame. *Simposium (International) on Combustion*, 615-623. 1998.

49 Watanabe, H. and Kendall, K., "Flame Spectrograms: I. Common Metals," Applied Spectroscopy, Vol. 9, No. 3, 1955, pp. 132–140.

50 Westbrook, C. and Dryer, F., "Simplified Reaction Mechanism for the Oxidation of Hydrocarbon Fuels in Flames," Combustion Science and Technology , Vol. 27, 1981, pp. 31–43.

51 Westbrook, C., & Dryer, F. Simplified Reaction Mechanism for the Oxidation of Hydrocarbon Fuels in Flames. *Combustion Science and Technology*. 1981.

52 Wilcox, C. Formulation of the k-w Turbulence Model Revisited. *AIAA Journal*. 2008.

53 Yang, V. and Anderson, W. E., Liquid Rocket Engine Combustion Instability, AIAA, Washington DC, 1995.

54 Yu, Y. C., Experimental and analytical investigations of longitudinal combustion instability in a continuously variable resonance combustor (CVRC), Ph.D. thesis. Purdue University, 2009.

55 Yu, Y., Sisco, J., Rosen, S., Madhav, A., & Anderson, W. Spontaneous Longitudinal Combustion Instability in a Continuously Variable Resonance Combustor. *Journal of Propulsion and Power.* 2012.

Addendum: Rotating Detonation Engine Combustion Study

Lab Task #: FA9550-14-1-0029 (106862)

Title: Rotating Detonation Engine Combustion Study

Reporting Period: 09/01/2014-08/31/2015

Laboratory Principal Investigator: William Anderson and Stephen Heister, Purdue University

Commercial Phone: 765-494-5126   **DSN:**   **FAX:** 765-494-0307

Mailing Address: Chaffee Hall, 500 Allison Road, West Lafayette, IN 47907

E-Mail Address: heister@purdue.edu

AFOSR Program Officer: Dr. Mitat Birkan

Research Objectives: Evaluate performance potential of the rotating detonation engine cycle for rocket propulsion applications using experimental platform with warm gaseous oxygen and hydrogen propellants.

Technical Summary:

This project was added on to existing project with Prof. Anderson that related to combustion stability in rocket combustors. Objectives for the portion of the work associated with rotating detonation combustion have been met with the creation of a high pressure rocket RDE combustor and the associated test campaigns. Figures 1 and 2 summarize the elements of the design. In addition, dynamic response of liquid injectors has been visualized in an optically-accessible rig that subjects an injection site to a passing detonation wave. Figures 3 and 4 summarize capabilities put in place for this rig. Extensive test campaigns were conducted in both facilities and documented in the attached conference publications. At present, we are preparing journal submissions based on this work.
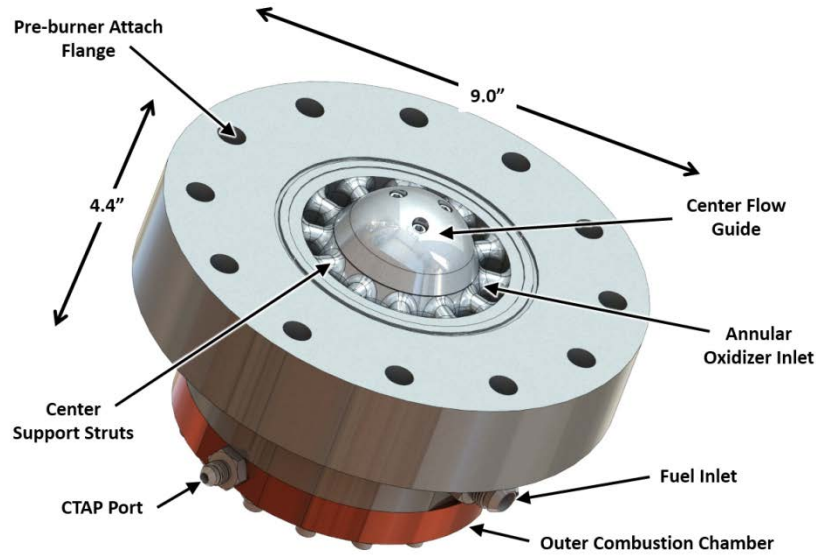
Figure 1: A perspective view of the RDE subassembly from the oxygen inlet side connected to the pre-burner.
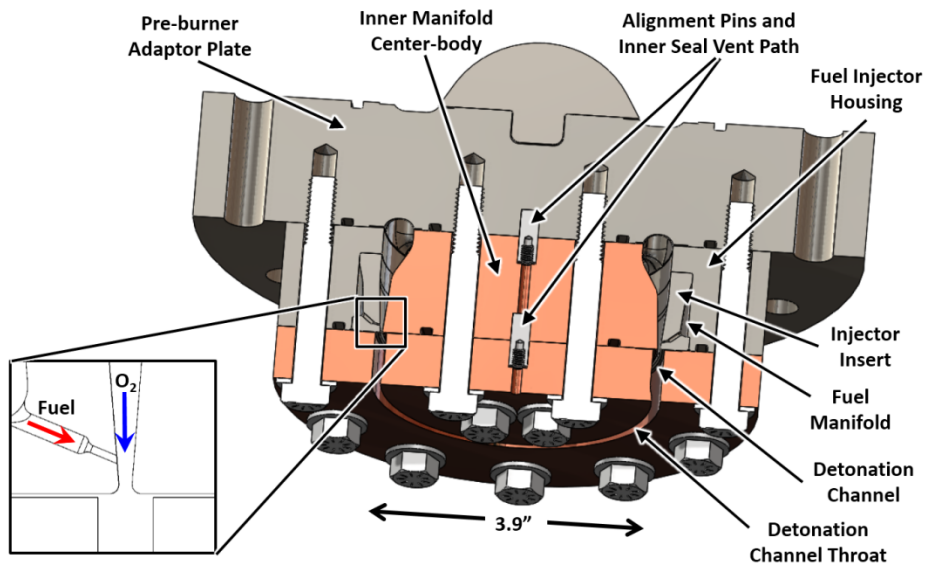
Figure 2: A section view of the RDE subassembly. The fuel and oxidizer flow path are highlighted on the left.
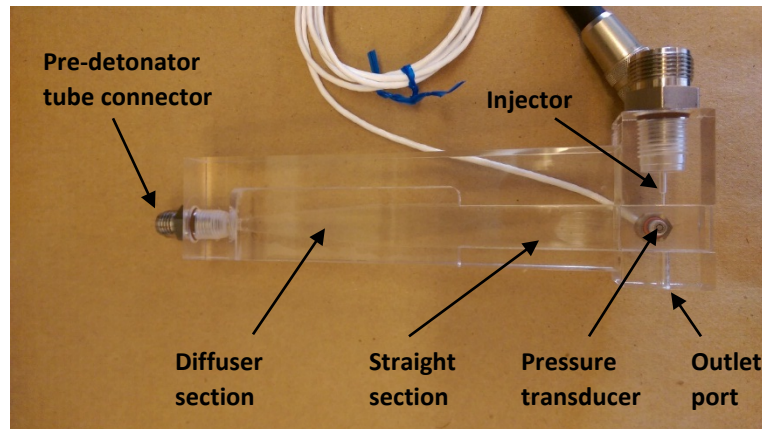
Figure 3. Close-up picture of optically-accessible test article for viewing liquid injection dynamic response to passing detonation front.

t = +0µs   t = +83µs   t = +166µs
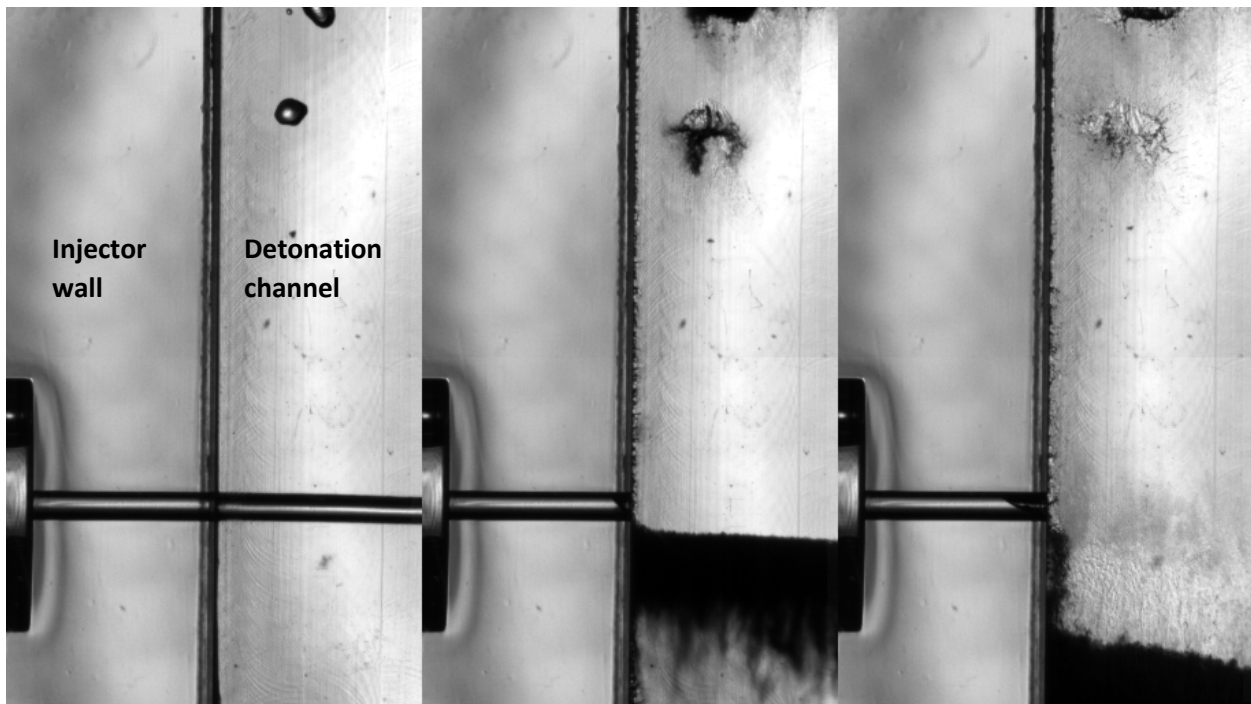
Figure 4. Wide view of sequenced still images showing break up of water jet during passage of detonation wave. Direction of wave passage is from top to bottom. Liquid flow is from left to right. Re ≈ 3500. Wide field images captured at 12,000 frames per second.

Budget Summary by Cost Category—Expenditure histories for the account are shown in the table below. All entries in table are fully burdened values including Purdue's 55% overhead rate. Travel expenditures were less than the $7.55K budgeted (burdened cost with 55% overhead rate) in the initial proposal however, supplies and expenses were substantially higher than the $28,720 budgeted (again fully burdened). Salary expenditures were correspondingly lower such that total expenditures match the total funds requested from AFOSR.

	Total Funds Received	FY14 Funds Received	FY15 Funds Received 10/1/14-8/31/15
Direct Labor Years and costs:			
Salary	$111.7	$9.3	$102.4
Supplies	$81.5	$6.8	$74.7
Travel	$5.4	$0.5	$5.0
Total Resource Requirements:	$198.6	$16.6	$182.0

Personnel Summary:

Personnel working the project include Prof. Heister and graduate students David Stechmann and Dasheng Lim.

Name	Degree	Discipline	% Time Involvement
Professor Stephen Heister	Ph.D.	Propulsion	10%
David Stechmann, Ph. D. student	M.S.	Propulsion	50%
Dasheng Lim, M.S. student	B. S.	Propulsion	50%

On-site Contractors: None

Visitors: None

Publication and Technical Reports Summary:

Publication of articles derived from the basic research effort should be listed chronologically in bibliography format. List only invention disclosures derived from the basic research effort. Honors may include recognition both inside and outside the Air Force S&T community.

Published in Peer Reviewed Journals, Books, etc: 0

Published in Un-reviewed Literature (e.g., Technical Proceedings):2

Accepted/Submitted for Publication:

Invention Disclosures and Patents Granted: Invited Lectures, Presentations, Talks, etc: 3 (AFRL, Edwards AFB, University of Michigan, European Conference on Space Sciences)

Professional Activities (editorships, conference & society committees, etc):

Honors Received (include lifetime honors such as Fellow, Honorary, Doctorates, etc—also state year elected: AIAA Fellow 2013

1.

1. Report Type

Final Report

Primary Contact E-mail
Contact email if there is a problem with the report.

wanderso@purdue.edu

Primary Contact Phone Number
Contact phone number if there is a problem with the report

765-496-2658

Organization / Institution name

Purdue

Grant/Contract Title
The full title of the funded effort.

High Fidelity Measurement and Modeling of Flames

Grant/Contract Number
AFOSR assigned control number. It must begin with "FA9550" or "F49620" or "FA2386".

FA9550-14-1-0029

Principal Investigator Name
The full name of the principal investigator on the grant or contract.

William E Anderson

Program Manager
The AFOSR Program Manager currently assigned to the award

Mitat Birkan

Reporting Period Start Date

12/01/2013

Reporting Period End Date

02/29/2016

Abstract

The defining characteristics of advanced chemical propulsion systems include very high rates of volumetric energy deposition, and very small combustor sizes. These characteristics give rise to extremely compact interactions in space and time between the chamber acoustic modes and unsteady heat release modes that may result in combustion instability. This project seeks to better understand the coupling mechanisms between heat release, hydrodynamics, and acoustics, and to develop tools to study the problem. High-fidelity simulations using large eddy simulations and reduced reaction kinetics are providing insight into unsteady reacting flows at an unprecedented level, providing some hope that a priori predictions will be possible in the next decade. Important questions include the accuracy of prediction that is required, and the level of modeling that is required for that prediction. The simulations must also be validated with experimental data. However, the time and length scales, and energy deposition rates in the canonical laboratory flames that have been studied over the past two decades are orders of magnitude different than the environments encountered in practical rocket combustors. The main objective of this study is to obtain high-fidelity experimental data critically needed to validate research codes at relevant conditions, and to develop systematic and rigorous means for comparison.

Distribution Statement
This is block 12 on the SF298 form. DISTRIBUTION A: Distribution approved for public release.

Explanation for Distribution Statement

If this is not approved for public release, please provide a short explanation. E.g., contains proprietary information.

SF298 Form

Please attach your SF298 form. A blank SF298 can be found here. Please do not password protect or secure the PDF The maximum file size for an SF298 is 50MB.

SF 298.pdf

Upload the Report Document. File must be a PDF. Please do not password protect or secure the PDF . The maximum file size for the Report Document is 50MB.

AFOSR_FinalReport_Anderson.pdf

Upload a Report Document, if any. The maximum file size for the Report Document is 50MB.

Archival Publications (published) during reporting period:

Tanabe, M. Saito, M., Hallum, W., Meier, E., Fuller, T., and Anderson, W., "Self-Excited Non-Linear Acoustic Wave in a Single-Element Model Rocket Combustor and its Influence on Flame," Transactions of the Japan Society for Aeronautical and Space Sciences, Vol. 14, (2016), pp. Pa_1-Pa_6.
Pomeroy, B., and Anderson, W., "Transverse Instability Studies in a Subscale Chamber," Journal of Propulsion and Power, doi: 10.2514/1.B35763.
Hardi, J., Hallum, W., Huang, C., and Anderson, W., "Approaches for Comparing Numerical Simulation of Combustion Instability and Flame Imaging," to appear in Journal of Propulsion and Power, doi: 10.2514/1.B35780.

Changes in research objectives (if any):

Change in AFOSR Program Manager, if any:

Extensions granted or milestones slipped, if any:

AFOSR LRIR Number

LRIR Title

Reporting Period

Laboratory Task Manager

Program Officer

Research Objectives

Technical Summary

Funding Summary by Cost Category (by FY, $K)

	Starting FY	FY+1	FY+2
Salary			
Equipment/Facilities			
Supplies			
Total			

Report Document

Report Document - Text Analysis

Report Document - Text Analysis

Appendix Documents

2. Thank You

E-mail user

May 17, 2016 13:26:05 Success: Email Sent to: wanderso@purdue.edu